An Unusual Case of Rapid Cyclogenesis in the northeast Pacific Basin: The Development and Influence of an Upper Level Jet/Front on Rapid Cyclogenesis

Jonathan E. Martin,[a] Patrick T. Beaty,[a] Andrew C. Winters,[b] Gary M. Lackmann[c]

[a] *University of Wisconsin-Madison*

[b] *University of Colorado-Boulder*

[c] *North Carolina State University*

Corresponding author: Jonathan E. Martin, jemarti1@wisc.edu

ABSTRACT

The influence of a developing upper-level jet/front system (ULJF) on a case of rapid cyclogenesis in the northeast Pacific basin in November 2019 is examined. The cyclogenesis proceeded in a "bottom up" fashion dominated initially by latent heat release associated with a diabatic Rossby wave (DRW) and subsequently by cyclonic vorticity advection (CVA) by the thermal wind at the downshear end of a strengthening ULJF. Differential subsidence served to increase both the horizontal temperature gradient and the geostrophic vorticity via tilting. Consequently, as the ULJF intensified so too did the elements directly associated with strengthening the CVA by the thermal wind thus instigating the rapid surface cyclogenesis.

The development of the ULJF is examined through analysis of QG omega fields calculated using different combinations of geopotential and thermal perturbations recovered from a piecewise potential vorticity (PV) inversion of the total PV. Tilting frontogenesis and geostrophic vorticity production via tilting are driven primarily by the upper-tropospheric winds acting on the upper-tropospheric and mean temperature fields. Less intense but nonetheless persistent and notable contributions to ULJF intensification were also made by elements of the circulation associated with the DRW. Thus, as in prior cases of such "bottom up" DRW rapid cyclogenesis, the upper tropospheric trigger in this case was actively shaped by the DRW life cycle. We suggest that the piecewise PV inversion-based QG omega perspective considered here offers novel insight into the influence of the DRW on ULJF intensification and, hence, on the subsequent period of rapid development.

SIGNIFICANCE STATEMENT

A rapidly-strengthening and record-setting storm system developed in late November 2019 near the U.S. West Coast and involved a rather strong atmospheric front in the upper atmosphere (called an 'upper front'). This storm system began in the lower atmosphere before the upper front moved over it and contributed substantially to further intensification. A localized region of sinking motion in the upper troposphere can result in strengthening of an upper front by increasing the horizontal temperature and wind speed gradients across the front. In our analysis, regions of localized sinking motion are directly attributed to processes in the lower, middle, and upper atmosphere. More analysis of this event is ongoing to further understand its peculiar nature.

1. Introduction

A recent analysis by Beaty et al. (2025) adopts a piecewise potential vorticity (PV) inversion perspective to describe the lifecycle of a record-setting extratropical cyclogenesis event that occurred over the relatively cold ocean surface of the northeast Pacific Ocean in late November 2019. They showed that the cyclone of interest began as a diabatic Rossby wave (DRW) mobilized by localized lower-tropospheric frontogenesis along a pre-existing baroclinic zone. After a period of eastward propagation characterized by little surface development, the cyclone began an extended period of rapid development upon becoming favorably aligned with an intensifying upper-level front that developed in north-northwesterly flow over the Gulf of Alaska. Though identified as a prominent feature in the lifecycle of the NV19 storm, the development of the upper-level front, and the piecewise contributions to that development, were not included in the Beaty et al. (2025) study. Instead, their analysis focused on elucidating the bottom-up sequencing that characterized the development by which near-surface PV dominated initial cyclogenesis, diabatically-induced PV controlled a prolonged interval of subsequent intensification, and upper-tropospheric PV characterized the final period of development.

At its core, lower-tropospheric cyclogenesis depends on the evacuation of mass from an atmospheric column which compels near-surface convergence and an associated spin-up of cyclonic vorticity. Thus, a non-uniform distribution of synoptic-scale vertical motion is necessary to instigate cyclogenesis. In one of the earliest dynamical treatments of the subject, Sutcliffe (1947) identified thermal wind advection of geostrophic vorticity as a primary forcing for the production of the requisite mid-latitude vertical motions. Subsequent investigations (e.g. Trenberth 1978; Hoskins et al. 1978; Martin 1998, Davies 2015) have reiterated this fundamental insight in a variety of alternative forms. Viewed from this dynamical perspective, insights into lower tropospheric cyclogenesis derive from understanding the origins of the associated upper-tropospheric vorticity features.

Reed and Sanders (1953) and Reed (1955) offered some of the first insights into this foundational problem in their consideration of upper-level frontogenesis. They showed that upper-level frontogenesis was characteristically associated with a folding of the tropopause whereby high PV air from the stratosphere was subducted, in a relatively thin sloping zone, into the upper to middle troposphere. Cross-stream variation in subsidence, with stronger sinking on the warm side of an originally weak or modest upper tropospheric baroclinic zone, tilted both isentropes and vortex tubes tied to vertical shear thereby simultaneously increasing the horizontal temperature gradient and the vertical vorticity along the developing frontal zone. Though controversial and considered so rare as to be marginalized at the time, the ubiquity of upper-level frontal zones – formed in this way and possessed of these characteristics – has been well established in the intervening decades (e.g., Newton 1954, 1958; Staley, 1960; Briggs and Roach, 1963; Danielsen, 1964,1968; Bosart, 1970; Shapiro, 1970, 1974, 1978, 1981, 1983). By virtue of their connection to the tropopause-level jet stream, such features have come to be known as upper-level jet front (ULJF) systems (Shapiro 1981).

Though not directly concerned with upper-level frontogenesis, Sanders' (1988) observational analysis of the life history of upper-tropospheric mobile troughs has a direct bearing on the present work. He found a preference for the development of such features in northwesterly flows quite like those in which ULJFs often develop. The implied connection between upper-level frontogenesis and the development of mid-tropospheric vorticity maxima was fortified by the idealized modeling study of Rotunno et al. (1994). Lackmann et al. (1997) investigated the development of the upper-level precursor disturbance associated with the IOP-2 storm during the Experiment on Rapidly Intensifying Cyclones in the Atlantic (ERICA). They found that tilting in northwesterly flow, in a region of cold air advection in cyclonic shear, generated an ULJF and an elongated mid-tropospheric vorticity strip. Diffluent flow in the associated jet exit region produced an isotropic "head" to the vortex feature at the downshear end of the ULJF and, consequently, lower tropospheric cyclogenesis. Lackmann et al. (1999), in an extension of their prior analysis, considered the same developing ULJF from the local energetics perspective (e.g., Orlanski and Katzfey 1991, Orlanski and Sheldon 1993). They found that upper-tropospheric ridges favor jet streak intensification via the Reynolds' stress as northerly perturbation flow to their east is often oriented within 45° of normal to the axis of dilatation of the time-mean flow. Thus, some fraction of the upper-tropospheric vorticity maxima routinely involved in lower tropospheric cyclogenesis are likely forged by upper-level frontogenesis – a suggestion that lends support and clarification to the provocative assertion made by Eliassen and Kleinschmidt (1957) that stratospheric air with high PV "is essentially the producing mass of cyclones." (p. 125).

The development of ULJFs preferentially occurs in the presence of geostrophic cold air advection in cyclonic shear (Keyser and Shapiro 1986), a synoptic circumstance that mobilizes what Rotunno et al. (1994) refer to as the "Shapiro effect" – the production of a transverse secondary ageostrophic circulation that encourages subsidence on the warm side of the developing upper-level front. Schultz and Doswell (1999) examined the development of ULJFs in southwesterly and northwesterly flow while Schultz and Sanders (2002) considered the birth of upper-level shortwave troughs in northwesterly flow in the context of ULJF development. In companion quasi-geostrophic and primitive equation simulations performed using an idealized channel model, Mudrick (1974) showed that the subsidence was predominantly a result of cyclonic vorticity advection (CVA) decreasing with height. A more recent examination of ULJF development by Martin (2014) showed that geostrophic cold air advection in cyclonic shear is physically identical to negative geostrophic shear vorticity advection by the thermal wind and that the associated subsidence (a form of shearwise, not transverse, ω) is the predominant source of frontogenetic tilting in the ULJF environment. Since tilting increases both the horizontal temperature gradient and the vertical vorticity along a quasi-2D frontal zone of finite length, the downshear end of that zone stands to experience a continual increase in cyclonic vorticity advection (CVA) by the thermal wind throughout the ULJF development period. In turn, the increasing CVA by the thermal wind, (also on the downshear end of the ULJF) , encourages more robust ascent, enhanced mass evacuation and intensified lower-tropospheric cyclogenesis.

Despite this intriguing physical connection, studies offering a detailed accounting of the manner by which ULJF development – and its thermodynamic and dynamic by-products – directly influence lower tropospheric cyclogenesis are exceedingly rare and those that exist view the interaction exclusively from the perspective of conservation of PV. Pioneering work by Bleck (1973) focused on the vortex tube stretching that occurs when a high PV feature aloft crosses to the warm side of a lower tropospheric baroclinic zone where the static stability is lower. His mechanistic explanation of the resulting cyclonic development clearly reflects elements of alternative explanations of the process presented in the basic state variables approach to development offered by, for instance, Sutcliffe (1947) and Petterssen (1956). Boyle and Bosart (1983) along with Uccellini et al. (1985), Whittaker et al. (1988), and Lackmann et al. (1999) come to similar conclusions regarding cases of high impact cyclogenesis considered from the PV perspective – essentially, cyclogenesis ensues when high PV air is advected over a poorly stratified lower troposphere.

In their seminal paper, Hoskins et al. (1985) revived interest in consideration of PV in the dynamical analysis of cyclone life cycles. Realization of the diagnostic possibilities described therein was provided by Davis and Emanuel (1991) who developed a computational scheme for PV inversion. A host of new insights have followed these important developments. Nonetheless, by virtue of the longstanding association of PV with the diagnosis of upper-level fronts and upper-level frontogenesis, the PV inversion perspective may have inadvertently forestalled clearer articulation of the relationship between the development of upper-level fronts and lower-tropospheric cyclogenesis afforded by the quasi-geostrophic theory. Presentation of such a perspective, mobilized to offer a physical explanation of the rapid development phase of the November 2019 (NV19) cyclone described by Beaty et al. (2025), is a focus of the present work.

Prior work has examined the interaction between DRWs and upper-tropospheric troughs (e.g. Wernli et al. 2002; Moore et al. 2008; Rivière et al. 2010; Boettcher and Wernli 2011, 2013; McKenzie 2014; Tamarin and Kaspi 2016; Zhang and Wang 2018). In their examination of storm Lothar, Wernli et al. (2002) concluded that the DRW played an active role in shaping the upper-tropospheric trough that subsequently provided the predominant forcing for the rapid cyclogenesis of Lothar. After analyzing a decade's worth of such storms while constructing a climatology of DRWs, however, Boettcher and Wernli (2013) suggested that most cases of explosive DRW development involve a DRW interacting with a *pre-existing* upper-tropospheric trough. No study of which we are aware has explicitly examined the development, and subsequent influence of, an ULJF in the context of a DRW explosive cyclogenesis event. Correspondingly, the influence of a DRW on the development of an ULJF that subsequently provides the forcing for rapid surface cyclogenesis has also been unexplored to date. Accordingly, the present paper examines aspects of both the influence of the ULJF system on the developmental life cycle of the November 2019 storm as well as the influences of the various pieces of the perturbation PV field (e.g., their balanced flow and thermal anomalies) on the development of the influential ULJF that characterized this case. The presentation begins in Section 2 with a short description of the data and the piecewise PV inversion method employed here. Section 3 provides a short synoptic description of the event emphasizing the role of the ULJF on the cyclogenesis. After establishing its substantial influence, Section 4 presents a quasi-geostrophic omega-based analysis of the ULJF development utilizing the kinematic and thermal anomaly fields derived from the piecewise PV inversion analysis of Beaty et al. (2025). Conclusions and suggestions for further analysis are offered in Section 5.

2. Data and Methods

2.1 Dataset

The primary dataset used in this study is the ECMWF reanalysis version 5 (ERA5; Hersbach et al. 2020) which contains data at a horizontal grid spacing of 0.25° x 0.25°. MSLP, wind speed and direction, temperature, geopotential height, and relative humidity on 19 vertical levels from 1000 hPa to 100 hPa (at 50 hPa intervals) were extracted at 1-hour intervals from 0000 UTC 1 November to 2300 UTC 31 December 2019 on a limited area domain extending from 10°N to 75°N and 180° to 90°W. The ERA5 data were then bilinearly interpolated to a 1.0° × 1.0° grid as coarse data with smooth gradients is more amenable to the PV inversion process (Hoskins et al. 1985) as well as the calculation of QG-omega (Martin 1999).

2.2 Piecewise PV inversion

Ertel (1942) expressed the potential vorticity, first formulated by Rossby (1940), as

$$EPV = -g(\zeta_\theta + f)\frac{\partial\theta}{\partial p},$$

where g is gravitational acceleration, ζ_θ is the isentropic relative vorticity, f is the planetary vorticity, $-\frac{\partial\theta}{\partial p}$ is a measure of the static stability, and *EPV* stands for Ertel PV. EPV is conserved for adiabatic, inviscid flow. Information about the flow associated with a distribution of EPV can be extracted through the process of PV inversion (Hoskins et al. 1985; Davis and Emanuel 1991). Details about the PV inversion method used in this study are described in depth in Beaty et al. (2025, their section 2b) and will not be repeated here in the interest of brevity.

In order that the PV inversion operation be accurately described as "piecewise", discrete pieces of the PV must be identified and inverted separately. The present work, derived as it is from the study of Beaty et al. (2025), follows a modified version of the piecewise partitioning described in Davis (1992), Korner and Martin (2000), and Winters and Martin (2017) which employs both isobaric and relative humidity criteria. The perturbation PV in this study is defined as the instantaneous PV minus the average PV over the interval 1 November – 31 December 2019, not a long-term climatology. An advantage of this approach is that it captures the background subseasonal flow pattern in which this cyclone developed. Other details of the partitioning scheme are described in Beaty et al. (2025) and result in three pieces of the perturbation PV; UPTROP (for the upper tropospheric PV, PV in unsaturated air in the 650 to 150 hPa layer), INT ("interior", for the diabatically-generated PV, PV in saturated air in the 950 to 150 hPa layer), and SFC (for the "surface" PV, PV in unsaturated air in the 950 to 700 hPa layer including perturbation θ on the bottom boundary of the domain). Finally, as in Beaty et al. (2025), inversion of the INT PV is not performed and geopotential height and streamfunction anomalies associated with that piece of the total perturbation PV are calculated as differences between the perturbation inversion values of each variable and the sum of the SFC and UPTROP values of each variable.

2.3 Quasi-geostrophic omega diagnostics

Gridded analyses from the piecewise PV inversion analysis, derived from the ERA5 dataset, are used in the calculation of quasi-geostrophic (QG) omega. The grid-point height and temperature data from these analyses were subjected to a Gaussian smoother that eliminates roughly two-thirds of the energy at wavelengths < 660 km, yielding results similar to those achieved using the cowbell filter described by Barnes et al. (1996) for use in QG diagnostics with mesoscale models. Employing the technique of successive over-relaxation (SOR), the *f*-plane version of the ***Q***-vector form of the QG-omega equation (Eq. 1) is solved using a spatially-averaged static stability that varies for each time with f_o set equal to the central latitude of the domain. Though calculations are made for each of the five species of QG-omega presented in Martin (2014)[1], the subsequent analyses focus only on the total QG-omega and conforms to solutions of (1)

$$\sigma\left(\nabla^2 + \frac{{f_o}^2}{\sigma}\frac{\partial^2}{\partial p^2}\right)\omega = -2\nabla \cdot \vec{Q} \qquad (1)$$

[1] These species include ω_n and ω_s, those QG ω fields derived from divergences of the across- and along-isentrope components of ***Q***, respectively. Calculations are also made of ω_{curv} and ω_{shear}, those QG ω fields derived from consideration of curvature and shear vorticity advections by the thermal wind, respectively.

where $\vec{Q}$ is given by $\vec{Q} = -\frac{R}{p}\left[\left(\frac{\partial \vec{V}_g}{\partial x} \cdot \nabla T\right)\hat{\imath}, \left(\frac{\partial \vec{V}_g}{\partial y} \cdot \nabla T\right)\hat{\jmath}\right]$. The piecewise PV inversion analysis of Beaty et al. (2025) isolated a mean PV, upper-tropospheric PV (UPTROP), a diabatically-generated PV (INT), and a near-surface PV which included lower boundary temperature anomalies (SFC). The sum of UPTROP, INT and SFC represented the FULL perturbation PV and inverting that for the balanced streamfunction and geopotential height fields returns what is referred to as the *perturbation inversion*. Adding the mean PV to the perturbation PV and inverting that sum results in what will be referred to as the *total inversion*. Inversion of each of these 4 pieces returned associated geopotential height and streamfunction fields, labeled Z_m (ψ_m), Z_{uptrop} (ψ_{uptrop}), Z_{int} (ψ_{int}), and Z_{sfc} (ψ_{sfc}), respectively. Since the geostrophic wind is defined as

$$\vec{V}_g = -\frac{g}{f_o}(\hat{k} \times \nabla Z), \qquad (2)$$

the geostrophic wind associated with each piece of the PV is returned by substituting the appropriate geopotential height field into (2). Similarly, the perturbation temperature associated with each discrete piece of geopotential can be determined via the hydrostatic relationship

$$\frac{\partial Z'}{\partial p} = \frac{-RT'}{gp},$$

where Z' and T' are the geopotential height and temperature associated with each of the four pieces of the total PV distribution defined earlier. The geostrophic wind and temperature anomalies associated with the various pieces of the total PV can be substituted into (1) to calculate $\boldsymbol{Q}$-vectors arising from interactions between the geostrophic wind associated with one piece of the PV and the thermal field associated with any other piece of the PV.

The total QG-omega can thus be partitioned into 16 distinct pieces (schematically illustrated in Fig. 1), each of which arises from forcing terms derived from the geostrophic winds and thermal fields associated with discrete portions of the total PV field as defined in the inversion process. A similar partitioning of the total QG-omega was used in Winters et al. (2020) to examine the production of vertical motions in the vicinity of jet superposition events. In subsequent portions of this analysis, the QG-omega associated with forcing derived from the UPTROP winds and the UPTROP thermal anomaly will, as illustrated in Fig. 1, be denoted as ω_{uu}. This conforms to the convention we employ in which the first subscript refers to the piece of the total PV from which the geostrophic winds in the associated forcing term originate (UPTROP) while the second points to the piece from which the thermal field derives (UPTROP).

3. Synoptic Description

By 0000 UTC 26 November a weak surface cyclone had emerged along the warm front of a weak stationary cyclone south of the Aleutian Islands (Fig. 2a). This new storm bisected a sprawling anticyclone that dominated the eastern north Pacific basin at this time. Upstream over the Bering Sea, a robust cyclone was still developing (not shown) and had a deep warm frontal zone that draped over western Alaska at this time, as evidenced by the notable 300:700 hPa thickness gradient there (Fig. 2b). An region of robust horizontal thermal contrast characterized a zonally-oriented baroclinic zone stretching eastward from southeast of Kodiak Island, AK to Haida Gwaii (formerly the Queen Charlotte Islands) off the coast of British Columbia. A modest geostrophic vorticity maximum of ~12 x 10^{-5} s^{-1} was embedded within the associated strong geostrophic vertical shear denting the 500 hPa ridge crest in the Gulf of Alaska (Fig. 2b). This vorticity maximum was located too far upstream of the nascent surface cyclone to contribute substantially to its development at this time as QG-omega attributable to CVA by the thermal wind (Sutcliffe 1947) – hereafter referred to as Sutcliffe omega[2] – associated with that feature was maximized well north of the surface cyclone (Fig. 2c). However, negative Sutcliffe omega at 700 hPa was located to the east of the cyclone center suggesting that CVA by the thermal wind in the lower troposphere was contributing to the storm's eastward propagation, consistent with its designation as a diabatic Rossby wave in the analysis of Beaty et al. (2025). A vertical cross-section through the Sutcliffe omega maxima at both levels (Fig. 2d) testifies to the fact that, at this time, the vertically disjointed distribution of upward vertical motion was not conducive to the deep column stretching characteristic of robust cyclogenesis.

Six hours later, the surface cyclone had deepened slightly (Fig. 3a) as the upper-level short wave encroached from the northwest (Fig. 3b). The mid-tropospheric baroclinicity associated with the warm front of the Bering Sea cyclone had modestly intensified by this time with more acute intensification nearer to the shortwave axis upstream of the surface cyclone (Fig. 3b). The 500 hPa geostrophic vorticity had assumed a more linear, northwest to southeast orientation by this time (Fig. 3b) with a particularly intense, quasi-isotropic feature at its southeastern terminus. This more concentrated upper-tropospheric feature was associated with intensified 500-hPa Sutcliffe omega that was still a bit too far removed to have a substantial impact on surface development at this time (Fig. 3c). Instead, the 700 hPa Sutcliffe omega was nearly collocated with the developing surface cyclone (Fig. 3c). A vertical cross-section through

[2] "Sutcliffe omega" (ω_{SUT}) refers to solution to the following form of the QG ω equation;

$$\sigma\left(\nabla^2 + \frac{{f_o}^2}{\sigma}\frac{\partial^2}{\partial p^2}\right)\omega_{SUT} = 2[f_o \frac{\partial \vec{V}_g}{\partial p} \cdot \nabla(\zeta_g + f)]$$

these two omega minima shows that the vertical disjuncture evident at 0000 UTC still characterized the development environment at this time (Fig. 3d).

In the ensuing six hours rapid surface development began as the sea-level pressure minima of the surface cyclone dropped 12 hPa to 1004 hPa (Fig. 4a). Simultaneously, the 500 hPa shortwave developed much stronger geostrophic vorticity at the southeastern end of a now contiguous vortex strip more perfectly positioned to support continued rapid development via CVA by the thermal wind (Fig. 4b). This stronger, more linear vortex structure was accompanied by even stronger mid-tropospheric baroclinicity than before, indicating that a potent upper-level jet front system (ULJF) had emerged in the north-northwesterly flow by this time. The combination of intensified baroclinicity coincident with an enhanced geostrophic vorticity gradient resulted in stronger 500 hPa Sutcliffe omega now located just about directly over the surface cyclone (Fig. 4c). The originally separate Sutcliffe ascent maxima at prior times were now nearly vertically juxtaposed (Fig. 4c and Fig. 4d) and much stronger than 12 hours before, resulting in a robust, increasingly vertical tropospheric-deep column of synoptic-scale ascent and surface cyclogenesis.

In the six hour period ending at 1800 UTC 26 November, the sea-level pressure minimum of the cyclone dropped 20 hPa to 984 hPa (Fig. 5a). The storm maintained a favorable orientation relative to the intensifying ULJF, which had developed a bulbous, isotropic nose at its southeastward extremity, that encouraged continued rapid development (Fig. 5b). By this time, the mid-tropospheric baroclinicity associated with the ULJF had greatly intensified and the feature now stretched nearly 2000 km across the eastern Gulf of Alaska. The 500 and 700 hPa Sutcliffe ascent maxima were almost perfectly coincident in the vertical at this time and located nearly directly above the SLP minima (Fig. 5c). A vertical cross-section through the ascent maximum emphasizes this coincidence and also illustrates the greater intensity of the QG-omega in the face of both the increased thermal wind and the increased vorticity gradient associated with the continued development of the ULJF (Fig. 5d).

An additional 12 hPa of central pressure fall occurred by 0000 UTC 27 November (Fig. 6a) by which time the cyclone was just off the coast of the California-Oregon border driving record wave heights and establishing SLP minimum records for the states of California and Oregon (Beaty et al. 2025). The storm was located at the base of a tropospheric-deep column of cyclonic geostrophic vorticity, the upper portion of which was contributed by the robust ULJF that had intensified and lengthened in the intervening 6 hours (Fig. 6b). Finally, the 500 and 700 hPa Sutcliffe ascent maxima were perfectly coincident and located just east of the surface cyclone center (Fig. 6c). A vertical cross-section through the ascent maxima at this time (Fig. 6d) emphasizes this cyclogenetic vertical phasing and suggests a vertical migration of the maximum ascent to higher elevation consistent with the greater influence of upper-levels in the development late in the life cycle as suggested by the analysis of Beaty et al. (2025).

4. Analysis

An ULJF, like all other frontal structures, must be characterized by local maxima in horizontal baroclinicity, cyclonic geostrophic vorticity, as well as large static stability. Given that fronts are quasi-linear features, in order to qualify as a frontal feature, the associated geostrophic vorticity maxima should also be notably anisotropic as well. ULJFs are important elements of a cyclogenetic environment as a consequence of their being characterized by large vorticity and large thermal contrast, a combination capable of providing robust forcing for vertical motion in the form of CVA by the thermal wind (Sutcliffe 1947; Martin 2006). As an individual ULJF progresses through its lifecycle, the vorticity and thermal structures often evolve dramatically via vertical tilting. Tilting of originally horizontally-oriented isentropes into a more vertical orientation is known as tilting frontogenesis and can be quantified by

$$\mathcal{F}_{tilt} = \frac{\partial \omega}{\partial n}\frac{\partial \theta}{\partial p} \tag{3}$$

where $\hat{n}$ is the natural coordinate direction pointing into the cold air (i.e. $\hat{n} = -\frac{\nabla\theta}{|\nabla\theta|}$) and ω is the vertical motion, $\frac{dp}{dt}$. Tilting can also impact the geostrophic vertical vorticity via

$$GeoVort_{tilt} = \hat{k} \cdot \left(\frac{\partial \vec{V}_g}{\partial p} \times \nabla\omega\right). \tag{4a}$$

And, since $\frac{\partial \vec{V}_g}{\partial p} = -\gamma\left(\hat{k} \times \nabla\theta\right)$, the prior expression can be written as

$$GeoVort_{tilt} = \gamma\left(\frac{\partial\theta}{\partial x}\frac{\partial\omega}{\partial x} + \frac{\partial\theta}{\partial y}\frac{\partial\omega}{\partial y}\right) = \gamma(\nabla\theta \cdot \nabla\omega) \tag{4b}$$

where $\gamma = \frac{R}{fp_o}\left(\frac{p_o}{p}\right)^{c_v/c_p}$ as in Eliassen (1962). Thus, to the extent that ω can be partitioned, so too can the tilting frontogenesis (3) as well as the geostrophic vorticity production via tilting (4).

Figure 7 shows 500 hPa geostrophic vorticity along with 300:700 hPa thickness at 5 different times during the evolution of the NV19 storm. It is clear, especially at the last four of these times (Figs. 7b, c, d, and e), that the geostrophic vorticity maximum was robustly linear and at least partly, and increasingly, coincident with the local maxima in thermal contrast. To be proven shortly, the coincident vorticity and thermal gradient maxima were also regions of high static stability at these four times. Thus, the subsequent analysis will examine aspects of the structure and dynamics of the ULJF at 0600, 1200, and 1800 UTC 26 November as well as at 0000 UTC 27 November 2019.

4.1 0600 UTC 26 November 2019

The ULJF was just beginning to emerge in the northwesterly flow over the central Gulf of Alaska by 0600 UTC 26 November. A vertical cross-section along AA-AA' (in Fig. 7b) indicated a robust baroclinic zone emerging from the upper-troposphere coincident with a fold in the dynamic tropopause (1.5 PVU isertel) at this time (Fig. 8a). Also shown in Fig. 8a is the QG-ω from the total inversion. The associated tilting frontogenesis (Fig. 8b) was only modestly frontogenetical at this time. The same vertical motion distribution also contributed to a tendency for geostrophic vorticity increase via tilting in exactly the same location (Fig. 8c). Since both the horizontal baroclinicity and the geostrophic relative vorticity were increasing via tilting, it is unsurprising that a robust couplet of 500 hPa CVA by the thermal wind straddled AA-AA' in the vicinity of the emerging ULJF (Fig. 8d).

The total tilting frontogenesis (Fig. 8b) can be further partitioned into contributions associated with the geostrophic flow and thermal perturbations attributable to the discrete PV anomalies considered in the piecewise PV inversion. Individual contributions to the tilting frontogenesis are made by 16 types of the QG-ω, each resulting from the interaction of one of four categories of geostrophic winds with one of the four categories of thermal distributions that constitute the piecewise PV inversion results (see Fig. 1 and accompanying text). Rather than present such partitioned pieces in a large collection of figures, we opt to show an example analysis at one time and then summarize the results of the partitioning at each of the four times in an abbreviated, tabular form that references the percentage contribution to the frontogenetical tilting (vorticity production via tilting) made by each piece of partitioned QG-omega acting on the total θ (or geostrophic wind) field.

Determination of the percentage contributions to both tilting frontogenesis and vorticity production via tilting made by the various species of QG-omega was computed by summing the values of each species' contribution at the black dots within the shaded portions of the tilting frontogenesis and vortex tilting maxima shown in panels (b) and (c) of Figs. 8, 11, 12 and 13. The yellow shaded areas enclose values of tilting frontogenesis (vortex tilting) exceeding 10 x 10^{-10} K m^{-1} s^{-1} (s^{-2}) except for the vortex tilting at 1200 UTC 26 November (Fig. 11b) where a bounding value of 20 x 10^{-10} s^{-2} was chosen as 10 x 10^{-10} s^{-2} extended far below the tropopause fold at that particular time and so was considered remote from the ULJF. At 0600 UTC it is apparent that the largest contribution to tilting frontogenesis associated with the ULJF was made by QG-omega forced by the combination of UPTROP winds acting on the mean and UPTROP perturbation temperature fields (i.e., the sum of ω_{um} and ω_{uu}) (Fig. 9a). The UPTROP winds acting on the INT and SFC temperature fields (ω_{ui} and ω_{us}) also made notable contributions (Fig. 9b). A slightly smaller contribution was made by the QG-omega arising from the interaction of the INT winds with the mean and UPTROP thermal fields (Fig. 9c). The contributions of each species to the total tilting frontogenesis at this time are indicated in Fig. 14a.

A similar partition of the forcing characterized the generation of geostrophic vorticity via tilting as shown in Fig. 10. The largest contribution to the total tilting vorticity tendency (shown in Fig. 8c) was provided by the UPTROP winds acting on the mean and UPTROP thermal fields (Fig. 10a) followed by the contribution made by ω_{mm} (Fig. 10b). A contribution was also made by the QG-omega arising from the interaction of INT winds and the mean thermal field (Fig. 10c). The contributions of each species to the total vorticity production via tilting at this time are shown in Fig. 15a.

4.2 1200 UTC 26 November 2019

The ULJF had undergone considerable development by 1200 UTC 26 November as both the horizontal temperature contrast and depth of the associated tropopause fold were more robust at this time (Fig. 11a). The total QG vertical motions were characterized by strong subsidence below 500 hPa straddled by weak ascent at higher elevations (Fig. 11a). This distribution produced stronger tilting frontogenesis at this time than at the previous six hours (Figs. 8b and 11b). Similarly stronger geostrophic vorticity tendency via tilting also occurred at this time (Fig. 11c). So, as had been the case six hours earlier, the ULJF continued to intensify as did its cyclogenetic potency as suggested by the stronger couplet of 500 hPa CVA by the thermal wind at this time (Fig. 11d).

Partitioning the total tilting frontogenesis into its various component contributions at this time reveals that the largest tilting frontogenesis was contributed by ω_{um} followed by nearly identical contributions by ω_{mm}, ω_{im} and ω_{us} (Fig. 14b). As had been the case six hours earlier, substantial contributions to the total geostrophic vorticity tendency via tilting were provided by ω_{mm}, and ω_{im} with the largest contribution coming from ω_{um} (Fig. 15b). The SFC wind was particularly uninvolved in both tilting frontogenesis and vortex tilting at this time.

4.3 1800 UTC 26 November 2019

The ULJF continued to strengthen through 1800 UTC 26 November with a strong horizontal temperature contrast penetrating to lower-levels of the troposphere (Fig. 12a) under the influence of a much more robust total QG-omega subsidence maxima. This descent forced stronger, more coherent tilting frontogenesis that penetrated downward to around 600 hPa at this time (Fig. 12b). Nearly coincident geostrophic vorticity tendency via tilting continued to encourage intensification of the upper-tropospheric geostrophic vorticity maxima at this time

(Fig. 12c). As before, the simultaneous strengthening of the vorticity and thermal contrasts fueled an even stronger couplet of CVA by the thermal wind at this time (Fig. 12d).

The partitioned tilting frontogenesis was different at 1800 UTC than at the prior times. The most substantial contribution to the total now came from ω_{um} (Fig. 14c) with notable contributions from both ω_{us} and ω_{im}. At this more well developed stage of the ULJF lifecycle, the distributions of ω_{mm} and ω_{mu} were quite hostile to intensification of the upper tropospheric temperature gradient. The main contributions to vorticity production via tilting were similar to those involved in tilting frontogenesis with the overwhelming contribution coming from ω_{um} (Fig. 15c). Less than half as large was the contribution from the sum of ω_{mm} and ω_{im} with support from ω_{ms} and ω_{us} (Fig. 15c). Interestingly, ω_{mm}, which discouraged tilting frontogenesis at this time, was contributing to vortex intensification.

4.4 0000 UTC 27 November 2019

By 0000 UTC 27 November, the ULJF had reached its maximum length and maximum intensity (see Figs. 6 and 7e) as the surface cyclone neared its minimum SLP. The thermal structure of the ULJF at this time was nearly indistinguishable from that which characterized it six hours earlier though the dynamic tropopause, as evidenced by the PV pendant associated with the ULJF, had descended to around 600 hPa by this time (Fig. 13a). The QG descent maximum had shifted decidedly toward the cold side of the front resulting in an abrupt recission of a slightly weaker tilting frontogenesis maximum to around 350 hPa by 0000 UTC (Fig. 13b). The tilting of geostrophic vertical shear into vertical vorticity had also weakened and retreated to higher elevation (Fig. 13c). Thus, by 0000 UTC 27 November, the intensification of the ULJF via tilting had effectively ended. Consequently, the couplet of 500 hPa CVA by the thermal wind had both weakened and become somewhat disorganized by this time (Fig. 13d).

The total tilting frontogenesis was, once again, largely forced by the combination of ω_{uu} and ω_{um} (Fig. 14d) with smaller contributions coming from the combination of ω_{ms}, ω_{us}, and ω_{im}. QG-omegas associated with INT temperature perturbations were discouraging of tilting frontogenesis at this time. The now weaker vortex tilting was still dominated by ω_{um} with ω_{uu} and ω_{us} making large contributions as well (Fig. 15d). As for the tilting frontogenesis at this time, QG-omegas associated with INT temperature perturbations were discouraging of vortex tilting, particularly so for ω_{ui}.

The analysis of the 18h period of ULJF development described above points to the dominance of tilting forced by ω_{um}, that is, QG-omega arising from the interaction of the UPTROP winds with the MEAN temperature field. This result suggests that ULJF development is particularly favored in regions where frequent passage of upper tropospheric circulation anomalies are coincident with robust, well established baroclinic zones characterized by a weekly to subseasonal presence. Such baroclinic zones are often characteristic of slowly evolving large-scale features in the cold season circulation such as a high amplitude ridge. The results presented here therefore provide novel dynamical support for the observed predominance of ULJF development in northwesterly flow on the downstream side of ridges.

Steady contributions from ω_{us} and ω_{im} persist throughout the analysis period as well. The contribution from ω_{us} suggests that the SFC temperature field, organized by the circulation associated with the DRW, plays some role in intensifying the ULJF thermal contrast. Similarly, the circulation associated with the diabatically generated PV (INT winds) interacting with the

MEAN temperature field also makes a persistent contribution to ULJF intensification. To the extent that the diabatic PV is a by-product of the DRW life-cycle, the role of ω_{im} represents another mechanism by which the DRW acted to intensify the ULJF in this case.

The vortex tilting partition appeared to operate slightly differently. A dependence on the MEAN thermal field is a common element it shares with the frontogenetic tilting though in this case it derives from the fact that the temperature gradient associated with a persistent baroclinic zone provides a background geostrophic vertical shear that is the circulation element that results in increased vertical vorticity via tilting. At every time in the analysis, ω_{um} does the largest share of vortex production via tilting pointing, again, to the importance of upper-level circulation anomalies traversing a comparatively stationary baroclinic zone to fashion cyclogenetic ingredients in the mid- to upper-troposphere. One other persistent contribution to vortex intensification via tilting came from ω_{us} suggesting, as for the ULJF evolution, that the SFC perturbation temperature (organized by the DRW) also had a role to play in upper tropospheric vortex intensification. This result highlights yet another example of the role of the DRW in facilitating the more substantial period of cyclogenesis that began after 1200 UTC 26 November.

Finally, it is important to consider other leading-order terms in both the frontogenesis and vorticity equations to establish the appropriateness of the focus on tilting that characterizes this analysis. Figure 16 examines the frontogenesis along the same cross-sections shown in Figs. 8, 11, 12, and 13 by adding the geostrophic frontogenesis ($F_{geo} = (\vec{Q} \cdot \nabla\theta)/|\nabla\theta|$) to the tilting frontogenesis already shown. In the range from ~300 to 600 hPa the tilting frontogenesis dominates in the vicinity of the ULJF from 0600 to 1800 UTC 26 November (Figs. 16a-c), becoming bit less robust by 0000 UTC 27 November (Fig. 16d).

The influence of vortex stretching ($[\zeta_g + f]\frac{\partial\omega}{\partial p}$) is compared to tilting in Fig. 17. Positive QG w is included in these analyses as well as its location in the vertical influences the level and intensity of the vortex stretching. When the subsidence is maximized at a high level, vortex stretching occurs above that level while the subsidence itself forces vortex tube tilting and below that level. Thus, the tilting term dominates in such instances (particularly so at 0600 and 1800 UTC 26 November, Figs. 17a and c). Even at 1200 UTC (Fig. 17b), when the subsidence is maximized around 850 hPa, the resulting stretching is less potent than the tilting. By 0000 UTC 27 November (Fig. 17d), there is substantial overlap in the vertical between the tilting and stretching contributions.

5. Summary and Conclusions

Surface cyclogenesis can proceed in a number of ways. When a nascent cyclonic disturbance is initiated along a low-level baroclinic zone the interactions between the associated cyclonic flow around the vortex and the baroclinic zone itself can provide sustained positive moisture and temperature advections downstream of the vortex. These advections contribute to the production of clouds and precipitation which, via the associated latent heat release, generate a lower-tropospheric cyclonic PV anomaly downstream, thereby appearing to propagate the original anomaly eastward. Such low-level developments were coined diabatic Rossby waves by Wernli et al. (2002) and, later, diabatic Rossby vortices by Moore and Montgomery (2004, 2005).

In late December 1999, storm Lothar devastated portions of western Europe, becoming the costliest windstorm in European history in terms of structural and ecological damage (Wernli et al. 2002). Focusing their analysis of the event on the evolution of Lothar as a DRW, Wernli et al. (2002) showed that Lothar underwent a 'bottom-up' development in which the lower tropospheric cyclonic PV anomaly (the DRW), acting on an initially zonal upper-tropospheric flow, induced upper-tropospheric trough development which eventually enabled a superposition of upper- and lower-tropospheric PV features that led to explosive development. Though bottom-up development of explosive DRWs with no pre-existing upper-tropospheric trough is rare (Boettcher and Wernli 2013), such a configuration served to initiate the mutual amplification of the two features which was manifest in the rapid development of Lothar.

Rapid lower tropospheric cyclogenesis is essentially driven by the sustained, quasi-isotropic, net column mass divergence that accompanies the development of strongly forced, mid-tropospheric, synoptic-scale vertical motions. Sutcliffe (1947) showed that on that scale a primary mechanism for forcing such vertical motions is cyclonic vorticity advection by the thermal wind, a result that has been robustly supported by subsequent work (e.g., Trenberth 1978; Hoskins et al. 1978; Martin 1998). The present paper has documented the influence of a developing ULJF on the case of rapid cyclogenesis off the California/Oregon coast in late November 2019 that was previously examined from the piecewise PV inversion perspective by Beaty et al. (2025).

ULJFs are well known synoptic-scale precursors to cyclogenesis as noted by a number of studies (e.g., Uccellini et al. 1985, Whittaker et al. 1988, Lackmann et al. 1997). The emphasis in many such studies has been to examine the resulting cyclogenesis as a consequence of circulation changes that ensue from the extrusion of high PV from the lower stratosphere into the less stably stratified upper- to middle-troposphere during ULJF development. This concept is the PV-thinking equivalent of the mechanism suggested by Petterssen and Smebye (1971) and referred to as Type B cyclogenesis – wherein an upper-level precursor disturbance sparks cyclogenesis upon crossing to the warm side of a lower tropospheric baroclinic zone. From the PV perspective, the argument relies more on the stability differences across the baroclinic zone than the thermal contrast in its conceptualization of the basic mechanisms of cyclogenesis.

A unique aspect of the NV19 storm examined here is that cyclogenesis began weakly as a DRW along a pre-existing, frontogenetically active warm front (Beaty et al. 2025). The strong ascent forced by the intense lower tropospheric frontogenesis, in concert with the large low-level vorticity characteristic of the frontal environment, produced, via stretching, exceptionally vorticity-rich air on the warm side of the lower tropospheric front. This same air underwent a second, separate vortex stretching episode when exposed to the strongly forced mid-tropospheric ascent that encroached from the northwest at the downshear end of the intensifying ULJF. The intensified thermal contrast and large vertical vorticity, both produced by the tilting required to strengthen the ULJF, conspired to produce the strongly forced upward vertical motions via CVA by the thermal wind.

In the present paper we have utilized the geostrophic wind and thermal fields associated with discrete portions of the total PV field as defined in the inversion process from Beaty et al. (2025) to investigate the development of the vigorous ULJF that lies at the heart of the mechanistic chain of events that drove this particular case of rapid cyclogenesis. The geostrophic wind and thermal fields recovered from the PV inversion process were used to calculate 16 separate pieces of the total QG-omega with the goal of delineating the separate influences of discrete portions of the total PV field on the subsidence responsible for the development of the ULJF. The differential subsidence forced tilting frontogenesis and geostrophic vorticity production via tilting in the upper-troposphere which encouraged intensification of the ULJF and its subsequent direct influence on the surface cyclogenesis via intensified CVA by the thermal wind.

Subsidence in the vicinity of the ULJF core, which led to an increase in horizontal baroclinicity and geostrophic relative vorticity within the ULJF region itself, primarily resulted from QG-omega produced by the UPTROP winds acting on the MEAN thermal field (Figs. 14 and 15). Throughout the period of analysis (0600 UTC 26 November – 0000 UTC 27 November), substantial contributions to both processes were also made by QG-omega forced by the UPTROP winds acting on the SFC temperature field along with INT winds acting on the MEAN temperature field (except for vorticity production via tilting at 1200 UTC (Fig. 15b)). With the exception of that associated with ω_{im}, the contribution to the vorticity and baroclinic intensification of the ULJF made by QG-omega species derived from the INT or SFC winds were negligible. Thus, though perhaps more subtly than was the case for Lothar (Wernli et al. 2002), it appears that in the present case the DRW that initiated cyclogenesis also played a role in shaping a potent upper-level precursor to the period of rapid cyclogenesis. Therefore it appears that this unusual surface cyclone was the product of consecutive periods of development, each influenced by distinct features whose subtle but discernible interaction conspired to produce this record setting event.

The analysis revealed that the NV19 storm shared a number of characteristics of so-called Type C cyclones (Plant et al. 2003; Ahmadi-Givi et al. 2004) – storms whose development is driven primarily by latent heat release and strong diabatic processes. Such cyclones are often initially triggered by a pre-existing upper-level PV anomaly over a region of weak low-level baroclinicity, frequently in maritime regions. These systems rely on moist processes to sustain growth, generating significant low- to mid-tropospheric positive PV anomalies (Gray & Dacre, 2006; Graf et al., 2017). Once developed, the diabatic PV feature can undergo a mutual amplification process with upper-tropospheric PV gradients as discussed by Davis and Emanuel (1991, see their Fig. 1c). Though Type C cyclones represent around a third of extratropical events and often remain non-developing or non-frontal in nature, they can (such as the cyclone in FASTEX IOP18, Cyclone Xynthia, and Cyclone Lothar historical cases) undergo explosive deepening, yielding wind damage, heavy precipitation, and strong warm conveyor belt activity (Ahmadi-Givi et al., 2004; Fink et al., 2012; Catto, 2016; Christ et al., 2026). Understanding the diabatic dynamics of these systems is critical to improving their representation in weather and climate models and in weather prediction (Dacre & Gray, 2013; Wernli & Gray, 2024).

Finally, the focus on CVA by the thermal wind as the forcing for the largest share of the QG-omega involved in the development can be further partitioned both in this individual case and more broadly to facilitate additional insight. Particularly, separate contributions from shear and curvature vorticity advections by the thermal wind are easily isolated (Martin 2015), as illustrated for one example time (1800 UTC 26 November) in Fig. 18. Though no conversions between geostrophic shear and curvature vorticities can be achieved by purely geostrophic flow (Bell and Keyser 1993), any given distribution of QG-omega is tied to an associated 3D distribution of ageostrophic winds which, in principle, can be isolated. Once identified, the influence of such ageostrophic winds on the geostrophic vorticity conversions likely operating during the development of the ULJF could then be investigated. Such work represents a natural extension of the present effort and is currently being undertaken with this case and another similar case of rapid development of a DRW over the northeast Pacific that occurred in November 2024.

Acknowledgments.

Chris Davis is acknowledged for developing the piecewise PV inversion code used in the analysis. This paper represents a portion of the second author's dissertation at the University of Wisconsin-Madison. The work was supported by the National Science Foundation under Grant AGS-1851152.

Data Availability Statement.

The fifth generation ECMWF atmospheric reanalysis dataset (ERA5) is produced by the Copernicus Climate Change Service (C3S) at ECMWF and can be accessed via https://cds.climate.copernicus.eu/cdsapp#!/dataset/10.24381/cds.143582cf?tab=overview. All computer programs written to perform the data analysis are available from the authors upon request.

REFERENCES

Ahmadi-Givi, F, G. C. Craig, and R. S. Plant, 2004: The dynamics of a midlatitude cyclone with very strong latent heat-release. *Quart. J. Roy. Meteor. Soc.*, **130**, 295–323.

Barnes, S. L., F. Caracena, and A. Marroquin, 1996: Extracting synoptic-scale diagnostic information from mesoscale models: The Eta model, gravity waves, and quasigeostrophic diagnostics. *Bulletin of the American Meteorological Society*, **77**, 519–528.

Beaty, P. T., J. E. Martin, A. C. Winters, and G. M. Lackmann, 2025: An Unusual Case of Rapid Cyclogenesis in the northeast Pacific Basin. Overview and Piecewise PV Inversion. *Monthly Weather Review*, **154**, https://doi.org/10.1175/MWR-D-24-0198.1.

Bjerknes, J., and H. Solberg, 1922: Life cycle of cyclones and the polar front theory of atmospheric circulation. *Geofys. Publ.*, **3**, 1–18.

Boettcher, M., and H. Wernli, 2011: Life cycle study of a diabatic Rossby wave as a precursor to rapid cyclogenesis in the North Atlantic—Dynamics and forecast performance. *Monthly Weather Review*, **139**, 1861–1878.

——, and ——, 2013: A 10-yr climatology of diabatic Rossby waves in the Northern Hemisphere. *Monthly weather review*, **141**, 1139–1154.

Catto, J. L., 2016: Extratropical cyclone classification and its use in climate studies. *Rev. of Geoph.,* **54**(2), 486-520.

Christ, S., Quinting, J., & Pinto, J. G., 2026: Characteristics of diabatically influenced cyclones with high wind damage potential in Europe. *Quarterly Journal of the Royal Meteorological Society*, **152**(776), e70083.

Davis, C. A., 1992: Piecewise potential vorticity inversion. *Journal of the atmospheric sciences*, **49**, 1397–1411.

——, and K. A. Emanuel, 1991: Potential vorticity diagnostics of cyclogenesis. *Monthly weather review*, **119**, 1929–1953.

Eliassen, A., 1962: On the vertical circulation in frontal zones. *Geofys. publ*, **24**, 147–160.

Ertel, H., 1942: Ein neuer hydrodynamischer wirbelsatz. *Meteorologische Zeitschrift*, **59**, 271–281.

Fink, A. H., S. Pohle, J. G. Pinto, and P. Knippertz, 2012: Diagnosing the influence of diabatic processes on the explosive deepening of extratropical cyclones. *Geophysical Research Letters*, *39*(7).

Fu, S., J. Sun, and J. Sun, 2014: Accelerating two-stage explosive development of an extratropical cyclone over the northwestern Pacific Ocean: A piecewise potential vorticity diagnosis. *Tellus A: Dynamic Meteorology and Oceanography*, **66**, 23210.

Graf, M.A., Wernli, H. and Sprenger, M., 2017. Objective classification of extratropical cyclogenesis. *Quart. J. Roy. Meteor. Soc*., **143**(703), pp.1047-1061.

Gray, S. L., and Dacre, H. F., 2006: Classifying dynamical forcing mechanisms using a climatology of extratropical cyclones. *Quart. J. Roy. Meteor. Soc.,* **132**, 1119-1137.

Heo, K.-Y., Y.-W. Seo, K.-J. Ha, K.-S. Park, J. Kim, J.-W. Choi, K. Jun, and J.-Y. Jeong, 2015: Development mechanisms of an explosive cyclone over East Sea on 3–4 April 2012. *Dynamics of Atmospheres and Oceans*, **70**, 30–46.

Hersbach, H., and Coauthors, 2020: The ERA5 global reanalysis. *Quart J Royal Meteoro Soc*, **146**, 1999–2049, https://doi.org/10.1002/qj.3803.

Hoskins, B. J., I. Draghici, and H. Davies, 1978: A new look at the ω-equation. *Quarterly Journal of the Royal Meteorological Society*, **104**, 31–38.

——, M. E. McIntyre, and A. W. Robertson, 1985: On the use and significance of isentropic potential vorticity maps. *Quarterly Journal of the Royal Meteorological Society*, **111**, 877–946.

Huo, Z., D.-L. Zhang, and J. R. Gyakum, 1999: Interaction of potential vorticity anomalies in extratropical cyclogenesis. Part I: Static piecewise inversion. *Monthly weather review*, **127**, 2546–2562.

Kohl, M., and P. A. O'Gorman, 2022: The Diabatic Rossby Vortex: Growth Rate, Length Scale and the Wave-Vortex Transition. *Journal of the Atmospheric Sciences*.

Korner, S. O., and J. E. Martin, 2000: Piecewise frontogenesis from a potential vorticity perspective: Methodology and a case study. *Monthly Weather Review*, **128**, 1266–1288.

Lackmann, G. M., D. Keyser, and L. F. Bosart, 1997: A characteristic evolution of upper-tropospheric cyclogenetic precursors during the Experiment on Rapidly Intensifying Cyclones over the Atlantic (ERICA). *Mon. Wea. Rev.*, **125,** 2529–2556.

_____, _____, and _____, 1999: Energetics of an intensifying midtropospheric jet streak during the Experiment on Rapidly Intensifying Cyclones over the Atlantic (ERICA). *Mon. Wea. Rev.,* **127**, 2777−2795.

Martin, J. E., 1998: The Structure and Evolution of a Continental Winter Cyclone. Part I: Frontal Structure and the Occlusion Process. *Mon. Wea. Rev.*, **126**, 303–328, https://doi.org/10.1175/1520-0493(1998)126<0303:TSAEOA>2.0.CO;2.

_____, 1999: Quasigeostrophic forcing of ascent in the occluded sector of cyclones and the trowal airstream. *Monthly weather review*, **127**, 70–88.

——, 2006: *Mid-latitude atmospheric dynamics: a first course*. John Wiley & Sons.

——, 2014: Quasi-geostrophic diagnosis of the influence of vorticity advection on the development of upper level jet-front systems. *Quarterly Journal of the Royal Meteorological Society*, **140**, 2658–2671.

McKenzie, M. W., 2014: *An analysis of numerical weather prediction of the diabatic Rossby Vortex*. NAVAL POSTGRADUATE SCHOOL MONTEREY CA.

Moore, R. W., M. T. Montgomery, and H. C. Davies, 2008: The integral role of a diabatic Rossby vortex in a heavy snowfall event. *Monthly weather review*, **136**, 1878–1897.

Newton, C. W., 1954: Frontogenesis and frontolysis as a three-dimensional process. *Journal of Atmospheric Sciences*, **11**, 449–461.

Plant, R.S., Craig, G.C. and Gray, S.L., 2003: On a threefold classification of extratropical cyclogenesis. *Quart. J. Roy. Meteor. Soc*., **129**, 2989-3012.

Reed, R. J., 1955: A study of a characteristic tpye of upper-level frontogenesis. *Journal of Atmospheric Sciences*, **12**, 226–237.

——, and F. Sanders, 1953: An investigation of the development of a mid-tropospheric frontal zone and its associated vorticity field. *Journal of Atmospheric Sciences*, **10**, 338–349.

——, and E. F. Danielsen, 1958: Fronts in the vicinity of the tropopause. *Archiv für Meteorologie, Geophysik und Bioklimatologie, Ser. A, Meteorologie und Geophysik*, **11**, 1–17.

Rivière, G., P. Arbogast, K. Maynard, and A. Joly, 2010: The essential ingredients leading to the explosive growth stage of the European wind storm Lothar of Christmas 1999. *Quarterly Journal of the Royal Meteorological Society: A journal of the atmospheric sciences, applied meteorology and physical oceanography*, **136**, 638–652.

Rossby, C.-G., 1940: Planetary flow patterns in the atmosphere. *Quarterly Journal of the Royal Meteorological Society*, **66**, 68–87.

Schultz, D.M. and Doswell III, C.A., 1999: Conceptual models of upper-level frontogenesis in south-westerly and north-westerly flow. *Quart. J. Roy. Meteor. Soc*., **125**, 2535-2556

_____, and Sanders, F., 2002. Upper-level frontogenesis associated with the birth of mobile troughs in northwesterly flow. *Mon. Wea. Rev.*, **130**(11), 2593-2610.

Shapiro, M. A., 1981: Frontogenesis and Geostrophically Forced Secondary Circulations in the Vicinity of Jet Stream-Frontal Zone Systems. *J. Atmos. Sci.*, **38**, 954–973, https://doi.org/10.1175/1520-0469(1981)038<0954:FAGFSC>2.0.CO;2.

Sutcliffe, R., 1947: A contribution to the problem of development. *Quarterly Journal of the Royal Meteorological Society*, **73**, 370–383.

Tamarin, T., and Y. Kaspi, 2016: The poleward motion of extratropical cyclones from a potential vorticity tendency analysis. *Journal of the Atmospheric Sciences*, **73**, 1687–1707.

Trenberth, K. E., 1978: On the interpretation of the diagnostic quasi-geostrophic omega equation. *Monthly Weather Review*, **106**, 131.

Wernli, H., S. Dirren, M. A. Liniger, and M. Zillig, 2002: Dynamical aspects of the life cycle of the winter storm 'Lothar'(24–26 December 1999). *Quarterly Journal of the Royal Meteorological Society: A journal of the atmospheric sciences, applied meteorology and physical oceanography*, **128**, 405–429.

_____, and S. L. Gray, 2024: The importance of diabatic processes for the dynamics of synoptic-scale extratropical weather systems–a review. *Wea .Clim. Dyn.*, **5**(4), 1299-1408.

Winters, A. C., and J. E. Martin, 2017: Diagnosis of a North American polar–subtropical jet superposition employing piecewise potential vorticity inversion. *Monthly Weather Review*, **145**, 1853–1873.

Zhang, G., and Z. Wang, 2018: North Atlantic extratropical Rossby wave breaking during the warm season: Wave life cycle and role of diabatic heating. *Monthly Weather Review*, **146**, 695–712.

FIGURES CAPTIONS

Fig. 1. Matrix illustrating the 16 separate QG-ω calculations resulting from combining each of the 4 wind components from the inversion with each of the 4 thermal components. Convention for each QG-ω species is that the 1st subscript refers to the geostrophic wind that was used and the 2nd subscript to the thermal component used to calculate the given QG-ω.

Fig. 2. (a) Sea level pressure isobars (solid blue, labeled in hPa and contoured every 4 hPa) and frontal locations (thick lines, red for warm front and blue for cold front) valid at 0000 UTC 26 November 2019. Position of the surface cyclone denoted by black "L". Green dashed lines are 950 hPa equivalent potential temperature (θ_e), labeled in K and contoured every 4 K. (b) 500 hPa geopotential heights (solid black contours, every 6 dam starting at 540 dam), 500 hPa geostrophic relative vorticity (solid blue contours, contoured every 4 x 10^{-5} s^{-1} starting at 8 x 10^{-5} s^{-1}), 300:700 hPa thickness (dashed red contours, contoured every 4.5 dam starting at 603 dam), and magnitude of 300:700 hPa thickness gradient (gray shading, shaded every 10 x 10^{-5} m m^{-1} starting at 40 x 10^{-5} m m^{-1}). (c) Blue lines are negative 500 hPa QG-omega attributable to CVA by the 300:700 hPa thermal wind ("Sutcliffe omega") contoured every -1 dPa s^{-1}. Red dashed lines are negative 700 hPa Sutcliffe omega contoured every -1 dPa s^{-1}. Black "L" as in (a). (d) Cross section along line A-A` in Fig. 2c of negative Sutcliffe omega contoured every -1 dPa s^{-1}. Red "X" indicates Sutcliffe omega minimum at 700 hPa and blue "X" indicates Sutcliffe omega minimum at 500 hPa.

Fig. 3. (a) As in Fig. 2a but for 0600 UTC 26 November 2019. (b) As in Fig. 2b but for 0600 UTC 26 November 2019. (c) As in Fig. 2c but for 0600 UTC 26 November 2019. Cross-section along line B-B` is shown in Fig. 3d. (d) As in Fig. 2d but for 0600 UTC 26 November 2019.

Fig. 4. (a) As in Fig. 2a but for 1200 UTC 26 November 2019. (b) As in Fig. 2b but for 1200 UTC 26 November 2019. (c) As in Fig. 2c but for 1200 UTC 26 November 2019. Cross-section along line C-C` is shown in Fig. 4d. (d) As in Fig. 2d but for 1200 UTC 26 November 2019.

Fig. 5. (a) As in Fig. 2a but for 1800 UTC 26 November 1843 2019. (b) As in Fig. 2b but for 1800 UTC 26 November 2019. (c) As in Fig. 2c but for 1800 UTC 26 November 2019. Cross-section along line D-D` is shown in Fig. 5d. (d) As in Fig. 2d but for 1800 UTC 26 November 2019.

Fig. 6. (a) As in Fig. 2a but for 0000 UTC 27 November 2019. (b) As in Fig. 2b but for 0000 UTC 27 November 2019. (c) As in Fig. 2c but for 0000 UTC 27 November 2019. Cross-section along line E-E` is shown in Fig. 6d. (d) As in Fig. 2d but for 0000 UTC 27 November 2019.

Fig. 7. (a) 300:700 hPa thickness and 500 hPa geostrophic relative vorticity fields valid at 0000 UTC 26 November 2019. Solid black lines are 300:700 hPa thickness in dm contoured every 4.5 dm starting at 576 dm. Solid, blue lines are 500 hPa geostrophic relative vorticity contoured every 4×10^{-5} s^{-1} starting at 8×10^{-5} s^{-1}. (b) As in (a) but valid for 0600 UTC 26 November 2019. Dashed box outlines region shown in Fig. 8d. Cross-section along line AA-AA` is shown in Figs. 8a-c. (c) As in (b) but valid for 1200 UTC 26 November 2019. Dashed box outlines region shown in Fig. 11d. Cross-section along line BB-BB` is shown in Figs. 11a-c. (d) As in (c) but valid for 1800 UTC 26 November 2019. Dashed box outlines region shown in Fig. 12d. Cross-section along line CC-CC` is shown in Figs. 12a-c. (e) As in (d) but valid for 0000 UTC 27 November 2019. Dashed box outlines region shown in Fig. 13d. Cross-section along line DD-DD` is shown in Figs. 13a-c.

Fig. 8. (a) Cross section along AA-AA' in Fig. 7b of the upper-level jet front system at 0600 UTC 26 November 2019. Solid, red lines are isentropes in K contoured every 3 K. Gray shading represents the total ω from the piecewise PV inversion with dark, solid gray indicating positive ω contoured every 1 dPa s^{-1} and light, dashed gray indicating negative ω contoured every -1 dPa s^{-1}. Dynamic tropopause, denoted by the 1.5 PV isertel, contoured in blue. (b) Tilting frontogenesis associated with the total ω in Fig. 8a contoured in solid blue every 2.5×10^{-10} K m^{-1} s^{-1} starting at 2.5×10^{-10} K m^{-1} s^{-1}. Thin gray lines are

isentropes as in Fig. 8a and thick gray line is the dynamic tropopause as in Fig. 8a. Values of the tilting frontogenesis at the black dots in the gray shaded area were used in the construction of Fig. 14a. (c) Geostrophic vorticity tendency via tilting associated with the total ω in Fig. 8a contoured in solid red every 2.5 x 10^{-10} s^{-2} starting at 2.5 x 10^{-10} s^{-2}. Thin and thick gray lines as in Fig. 8b. Values of the vorticity tendency via tilting at the black dots in the gray shaded region were used in the construction of Fig. 15a. (d) 500 hPa geostrophic vorticity advection by the 300:700 hPa thermal wind. Solid blue (dashed red) contours represent NVA (PVA) labeled in m kg^{-1} s^{-1} and contoured every 2 x 10^{-17} m kg^{-1} s^{-1}. Solid black line is cross-section line AA-AA`.

Fig. 9. (a) Tilting frontogenesis accomplished by ω_{um} and ω_{uu} valid at 0600 UTC 26 November 2019 contoured in solid orange every 2.5 x 10^{-10} K m^{-1} s^{-1} starting at 2.5 x 10^{-10} K m^{-1} s^{-1}. Light gray shading is tilting frontogenesis from the total ω as in Fig. 8b. Thin gray lines are isentropes as in Fig. 8a. (b) Tilting frontogenesis accomplished by ω_{mm} valid at 0600 UTC 26 November 2019 contoured in solid green every 2.5 x 10^{-10} K m^{-1} s^{-1} starting at 2.5 x 10^{-10} K m^{-1} s^{-1}. Light gray shading and thin gray lines as in Fig. 9a. (c) Tilting frontogenesis accomplished by the sum of ω_{im} and ω_{iu} valid at 0600 UTC 26 November 2019 contoured in solid pink every 2.0 x 10^{-10} K m^{-1} s^{-1} starting at 2.0 x 10^{-10} K m^{-1} s^{-1}. Light gray shading and thin gray lines as in Fig. 9a.

Fig. 10. (a) Geostrophic vorticity tendency via tilting accomplished by ω_{um} and ω_{uu} valid at 0600 UTC 26 November 2019 contoured in solid orange every 2.5 x 10^{-10} s^{-2} starting at 2.5 x 10^{-10} s^{-2}. Light gray shading is geostrophic vorticity tendency via tilting from the total ω as in Fig. 8c. Thin gray lines are isentropes as in Fig. 8a. (b) Geostrophic vorticity tendency via tilting accomplished by ω_{mm} valid at 0600 UTC 26 November 2019 contoured in solid green every 2.5 x 10^{-10} s^{-2} starting at 2.5 x 10^{-10} s^{-2}. Light gray shading and thin gray lines as in Fig. 10a. (c) Geostrophic vorticity tendency via tilting accomplished

by ω_{im} valid at 0600 UTC 26 November 2019 contoured in solid pink every 2.5 x 10^{-10} s^{-2} starting at 2.5 x 10^{-10} s^{-2}. Light gray shading and thin gray lines as in Fig. 10a.

Fig. 11. Cross section along BB-BB' in Fig. 7c of the upper-level jet front system at 1200 UTC 26 November 2019. (a) As in Fig. 8a but for 1200 UTC 26 November 2019. (b) As in Fig. 8b but for 1200 UTC 26 November 2019. (c) As in Fig. 8c but for 1200 UTC 26 November 2019. (d) As in Fig. 8d but for 1200 UTC 26 November 2019.

Fig. 12. Cross section along CC-CC' in Fig. 7d of the upper-level jet front system at 1800 UTC 26 November 2019. (a) As in Fig. 8a but for 1800 UTC 26 November 2019. (b) As in Fig. 8b but for 1800 UTC 26 November 2019. (c) As in Fig. 8c but for 1800 UTC 26 November 2019. (d) As in Fig. 8d but for 1800 UTC 26 November 2019.

Fig. 13. Cross section taken along DD-DD' in Fig. 7e of the upper-level jet front system at 0000 UTC 27 November 2019. (a) As in Fig. 8a but for 0000 UTC 27 November 2019. (b) As in Fig. 8b but for 0000 UTC 27 November 2019. (c) As in Fig. 8c but for 0000 UTC 27 November 2019. (d) As in Fig. 8d but for 0000 UTC 27 November 2019.

Fig. 14. (a) Percentage contribution of total tilting frontogenesis by QG-omega species along line AA-AA' in Fig. 7b at 0600 UTC 26 November 2019. (b) As for Fig. 14a but as measured along line BB-BB' in Fig. 7c at 1200 UTC 26 November 2019. (c) As for Fig. 14a but as measured along line CC-CC' in Fig. 7c at 1800 UTC 26 November 2019. (d) As for Fig. 14a but as measured along line DD-DD' in Fig. 7e at 0000 UTC 27 November 2019.

Fig. 15 (a) Percentage contribution of total vorticity production via tilting by QG-omega species along line AA-AA' in Fig. 7b at 0600 UTC 26 November 2019. (b) As for Fig. 15a but as measured along line BB-BB' in Fig. 7c at 1200 UTC 26 November 2019. (c) As for Fig. 15a but as measured along line CC-CC' in Fig. 7c at 1800 UTC 26 November 2019. (d) As for Fig. 15a but as measured along line DD-DD' in Fig. 7e at 0000 UTC 27 November 2019.

Fig. 16 (a) Tilting frontogenesis (dark gray), total 3D geostrophic frontogenesis (red for negative, blue for positive), theta (light gray) and 1.5 PVU isertel along the cross-section shown in Fig. 8c at 0600 UTC 26 November. (b) As for Fig. 16a but for 1200 UTC 26 November along the cross section line shown in Fig. 11c. (c) As for Fig 16a but for 1800 UTC 26 November along the cross-section line shown in Fig. 12c. (d) As for Fig. 16a but for 0000 UTC 27 November along the cross-section line shown in Fig. 13c. Frontogenesis is shown in units of 10^{-10} K m^{-1} s^{-1} and contoured every 2.5 x 10^{-10} K m^{-1} s^{-1}.

Fig. 17 (a) Tilting vorticity tendency (green), stretching tendency (red), theta (light gray) and QG subsidence (positive omega, dashed blue) along the cross-section shown in Fig. 8c at 0600 UTC 26 November. Vorticity tendencies in units of 5 x 10^{-10} s^{-2}. (b) As for Fig. 17a but for 1200 UTC 26 November along the cross section line shown in Fig. 11c. (c) As for Fig 17a but for 1800 UTC 26 November along the cross-section line shown in Fig. 12c. (d) As for Fig. 17a but for 0000 UTC 27 November along the cross-section line shown in Fig. 13c.

Fig. 18 (a) 500 hPa geostrophic vorticity advection by the 300:700 hPa thermal wind at 1800 UTC 26 November 2019. PVA (NVA) by the thermal wind indicated by the dashed red (solid blue) contours labeled in m kg^{-1} s^{-1} and contoured every 2.5 x 10^{-17} m kg^{-1} s^{-1} starting at 2.5 x 10^{-17} m kg^{-1} s^{-1} (-2.5 x 10^{-17} m kg^{-1} s^{-1}). "L" indicates position of sea-level pressure minimum at 1800 UTC 26 November 2019. (b) As for Fig. 18a but for 500 hPa geostrophic shear vorticity advection by the 300:700 hPa thermal wind. Isopleths labeled and contoured as in Fig. 18a. (c) As for Fig. 18a but for 500 hPa geostrophic curvature vorticity advection by the 300:700 hPa thermal wind. Isopleths labeled and contoured as in Fig. 18a.

ω_{mm}	ω_{mu}	ω_{mi}	ω_{ms}	*MEAN* $\boldsymbol{V_g}$
ω_{um}	ω_{uu}	ω_{ui}	ω_{us}	*UPTROP* $\boldsymbol{V_g}$
ω_{im}	ω_{iu}	ω_{ii}	ω_{is}	*INT* $\boldsymbol{V_g}$
ω_{sm}	ω_{su}	ω_{si}	ω_{ss}	*SFC* $\boldsymbol{V_g}$
MEAN ***T***	*UPTROP* ***T***	*INT* ***T***	*SFC* ***T***	

Fig. 1. Matrix illustrating the 16 separate QG-omega calculations resulting from combining each of the 4 wind components from the inversion with each of the 4 thermal components. Convention for each QG-omega species is that the 1st subscript refers to the geostrophic wind that was used and the 2nd subscript to the thermal component used to calculate the given QG-omega.

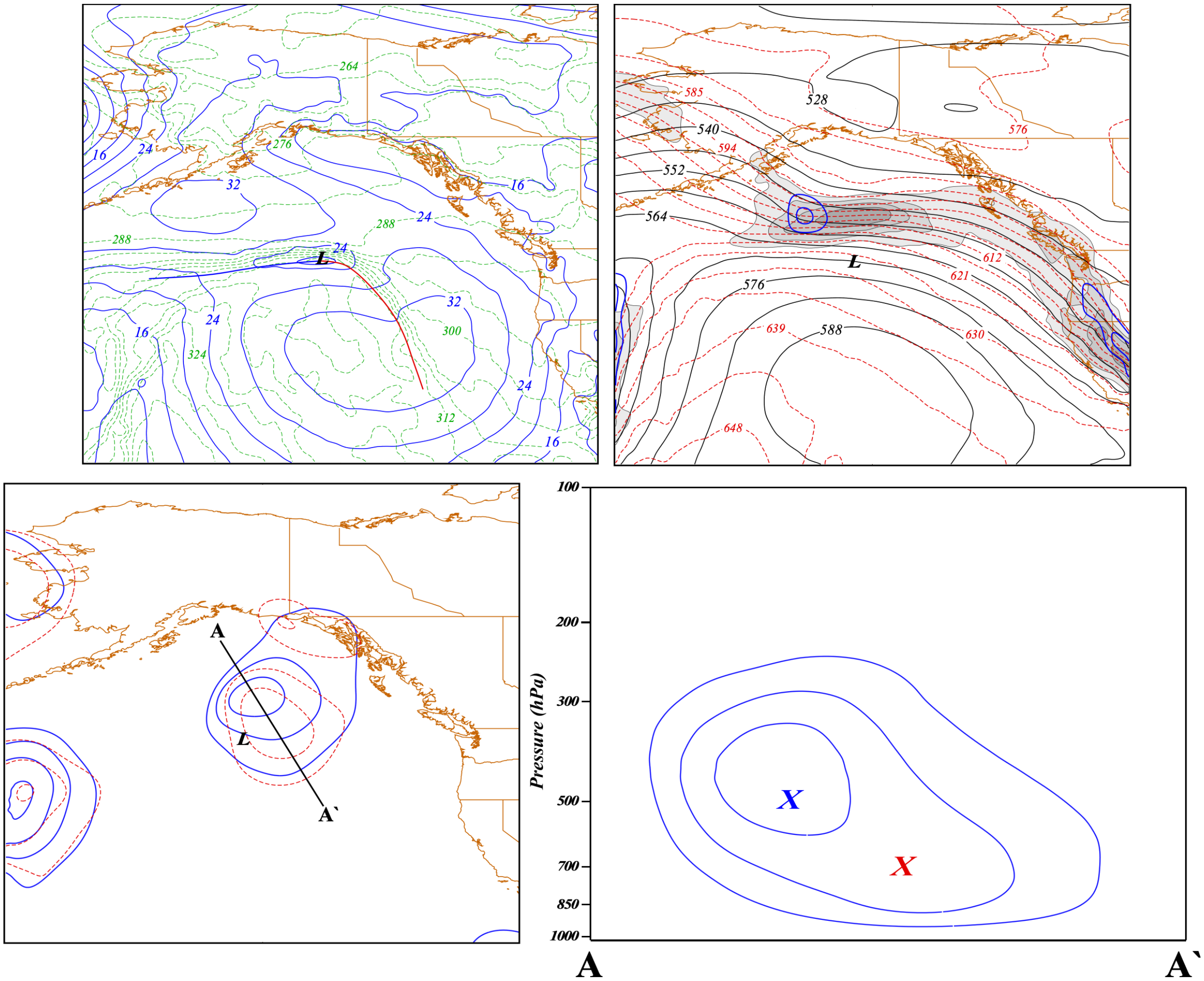

Fig. 2. (a) Sea level pressure isobars (solid blue, labeled in hPa and contoured every 4 hPa) and frontal locations (thick lines, red for warm front and blue for cold front) valid at 0000 UTC 26 November 2019. Position of the surface cyclone denoted by black "L". Green dashed lines are 950 hPa equivalent potential temperature (θ_e), labeled in K and contoured every 4 K. (b) 500 hPa geopotential heights (solid black contours, every 6 dam starting at 540 dam), 500 hPa geostrophic relative vorticity (solid blue contours, contoured every 4×10^{-5} s^{-1} starting at 8×10^{-5} s^{-1}), 300:700 hPa thickness (dashed red contours, contoured every 4.5 dam starting at 603 dam), and magnitude of 300:700 hPa thickness gradient (gray shading, shaded every 10×10^{-5} m m^{-1} starting at 40×10^{-5} m m^{-1}). (c) Blue lines are negative 500 hPa QG-omega attributable to CVA by the 300:700 hPa thermal wind ("Sutcliffe omega") contoured every -1 dPa s^{-1}. Red dashed lines are negative 700 hPa Sutcliffe omega contoured every -1 dPa s^{-1}. Black "L" as in (a). (d) Cross section along line A-A` in Fig. 2c of negative Sutcliffe omega contoured every -1 dPa s^{-1}. Red "X" indicates Sutcliffe omega minimum at 700 hPa and blue "X" indicates Sutcliffe omega minimum at 500 hPa.

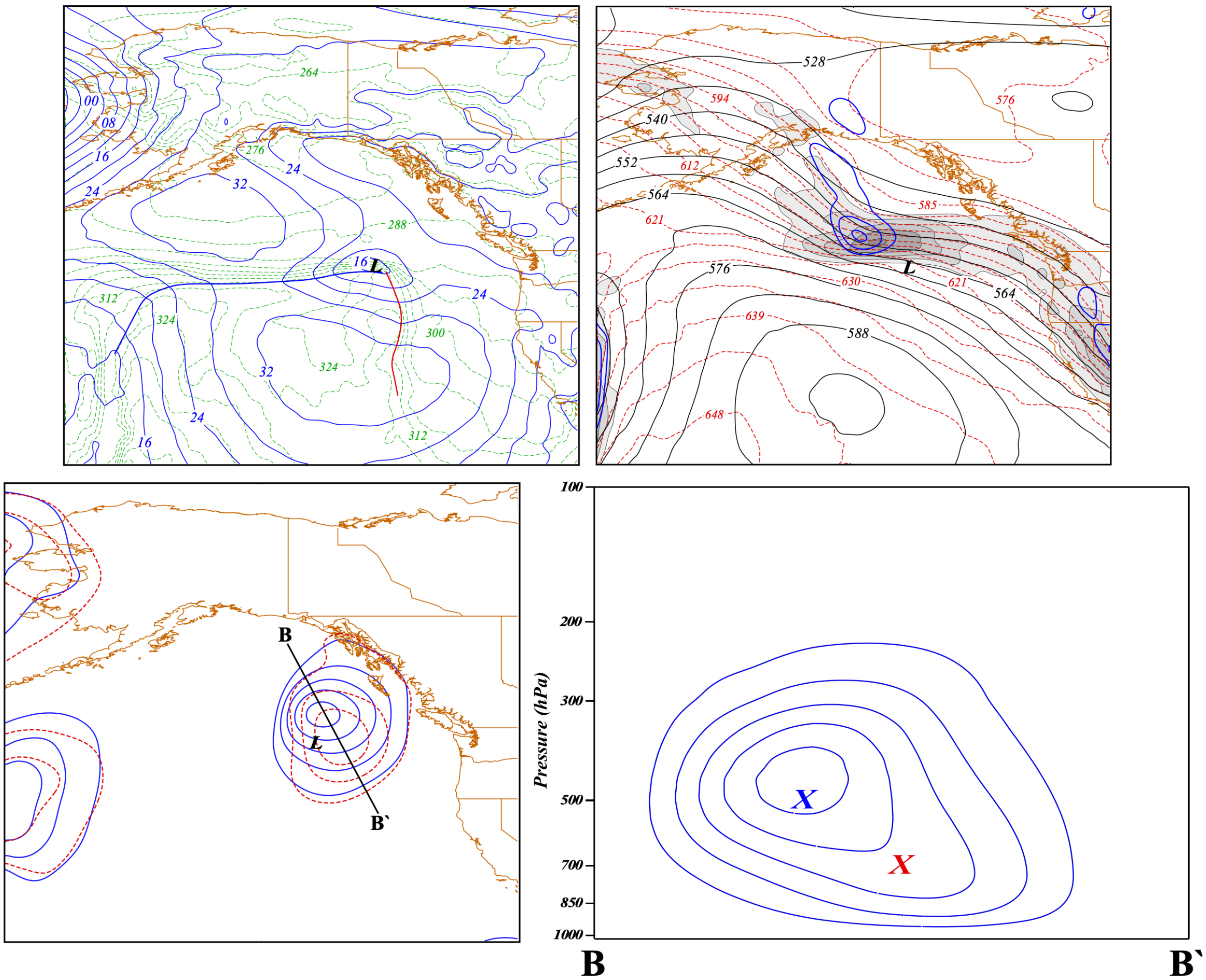

Fig. 3. (a) As in Fig. 2a but for 0600 UTC 26 November 2019. (b) As in Fig. 2b but for 0600 UTC 26 November 2019. (c) As in Fig. 2c but for 0600 UTC 26 November 2019. Cross-section along line B-B` is shown in Fig. 3d. (d) As in Fig. 2d but for 0600 UTC 26 November 2019.

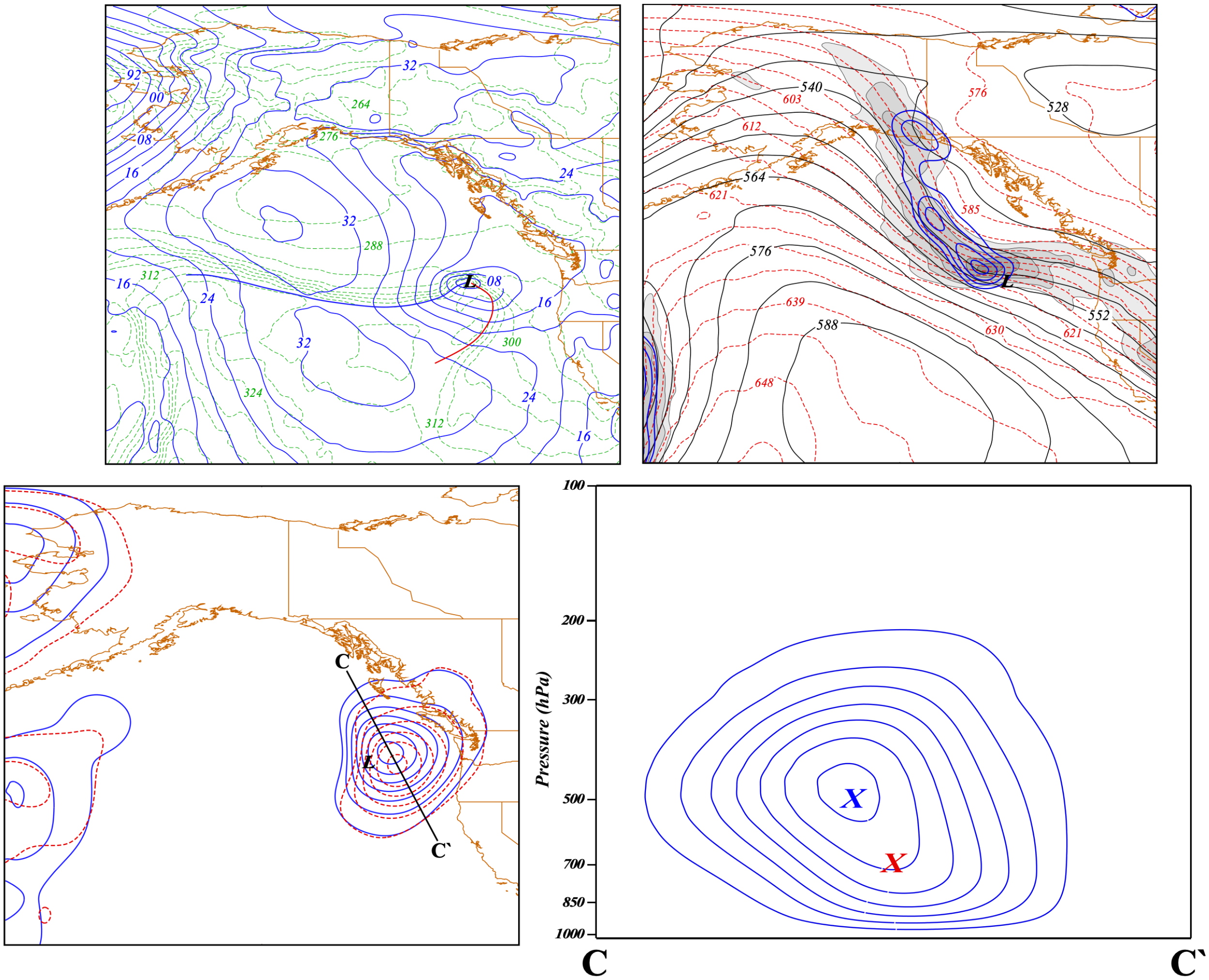

Fig. 4. (a) As in Fig. 2a but for 1200 UTC 26 November 2019. (b) As in Fig. 2b but for 1200 UTC 26 November 2019. (c) As in Fig. 2c but for 1200 UTC 26 November 2019. Cross-section along line C-C` is shown in Fig. 4d. (d) As in Fig. 2d but for 1200 UTC 26 November 2019.

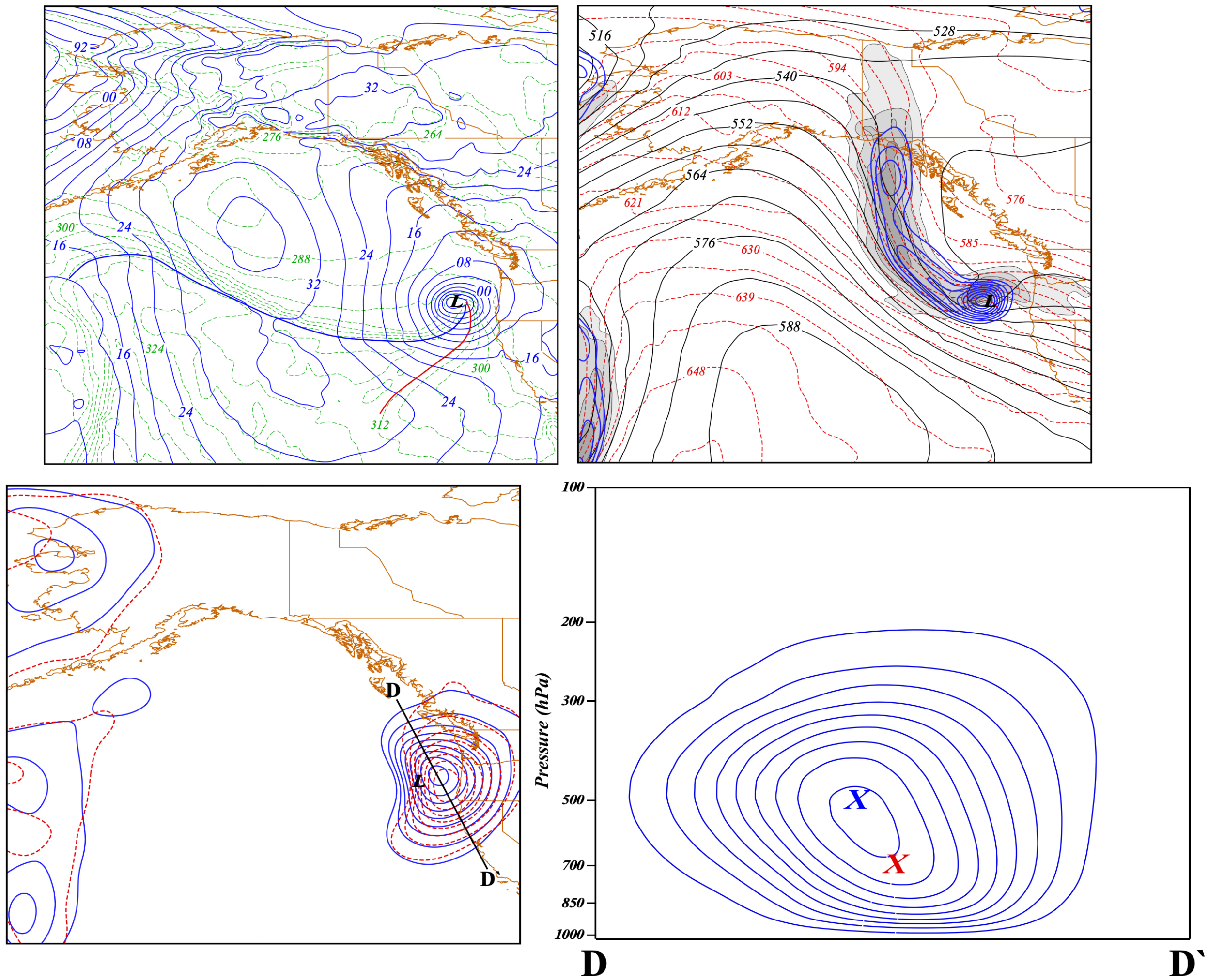

Fig. 5. (a) As in Fig. 2a but for 1800 UTC 26 November 1843 2019. (b) As in Fig. 2b but for 1800 UTC 26 November 2019. (c) As in Fig. 2c but for 1800 UTC 26 November 2019. Cross-section along line D-D` is shown in Fig. 5d. (d) As in Fig. 2d but for 1800 UTC 26 November 2019.

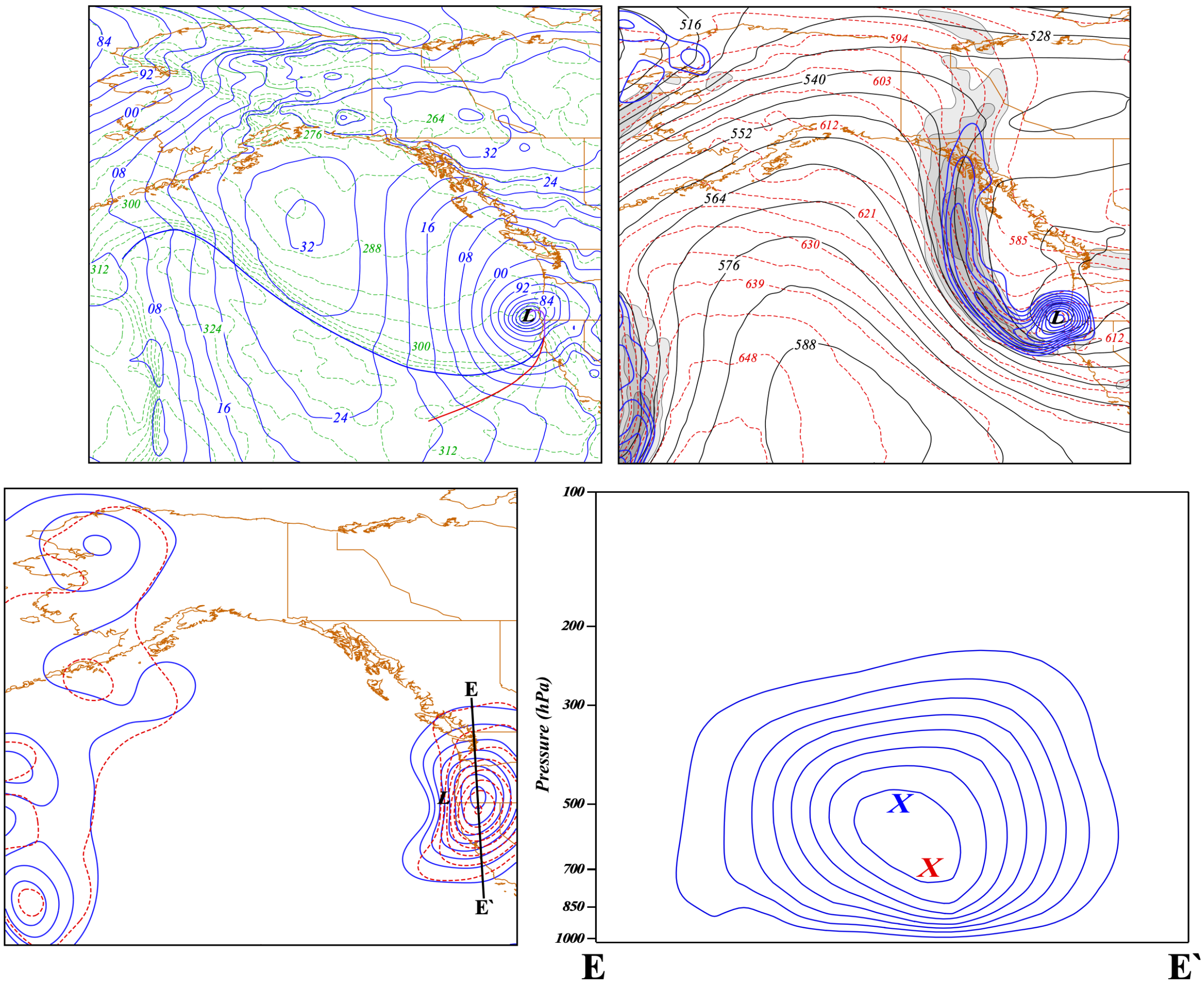

Fig. 6. (a) As in Fig. 2a but for 0000 UTC 27 November 2019. (b) As in Fig. 2b but for 0000 UTC 27 November 2019. (c) As in Fig. 2c but for 0000 UTC 27 November 2019. Cross-section along line E-E` is shown in Fig. 6d. (d) As in Fig. 2d but for 0000 UTC 27 November 2019.

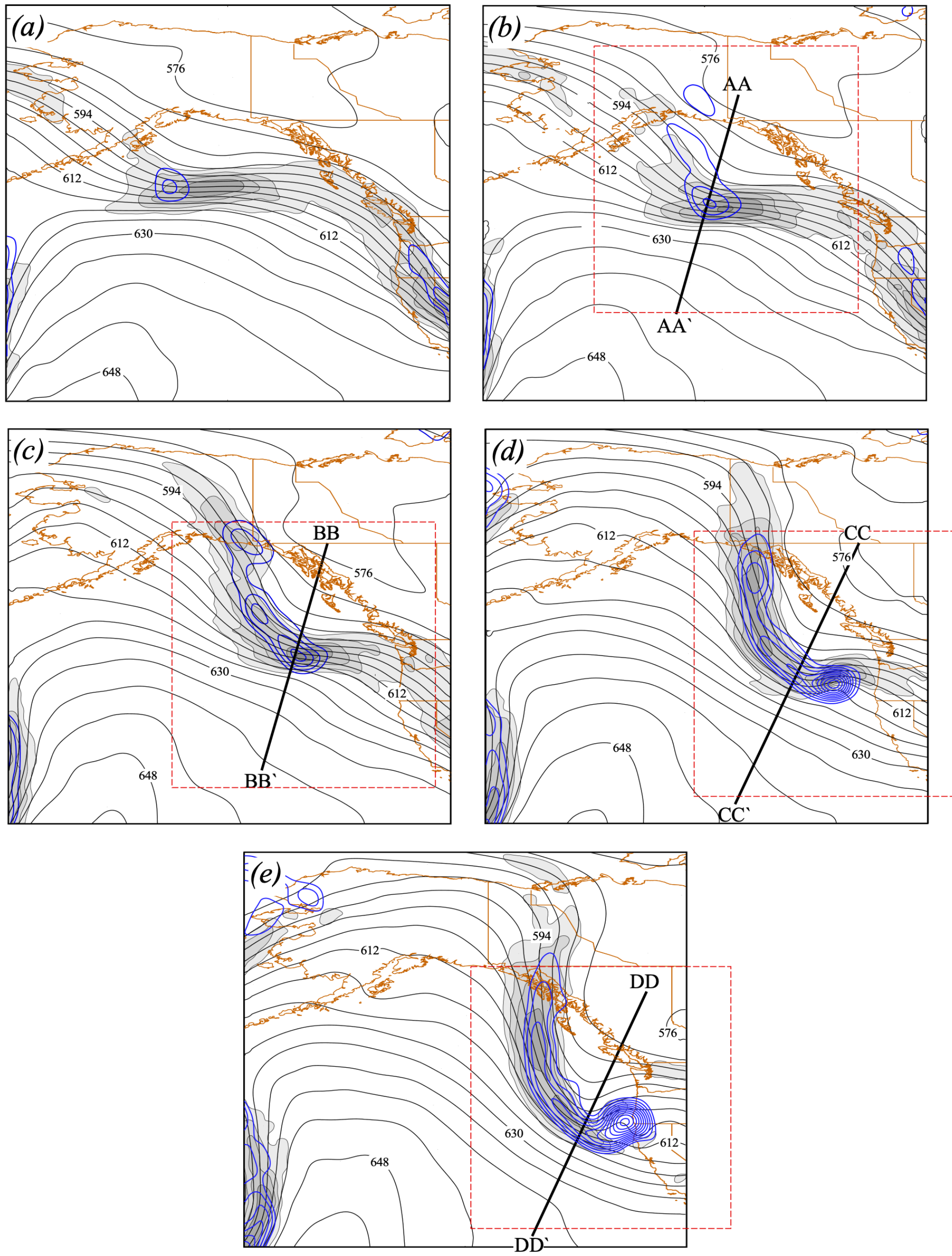

Fig. 7. (a) 300:700 hPa thickness and 500 hPa geostrophic relative vorticity fields valid at 0000 UTC 26 November 2019. Solid black lines are 300:700 hPa thickness in dm contoured every 4.5 dm starting at 576 dm. Solid, blue lines are 500 hPa geostrophic relative vorticity contoured every 4×10^{-5} s^{-1} starting at 8×10^{-5} s^{-1}. (b) As in (a) but valid for 0600 UTC 26 November 2019. Dashed box outlines region shown in Fig. 8d. Cross-section along line AA-AA` is shown in Figs. 8a-c. (c) As in (b) but valid for 1200 UTC 26 November 2019. Dashed box outlines region shown in Fig. 11d. Cross-section along line BB-BB` is shown in Figs. 11a-c. (d) As in (c) but valid for 1800 UTC 26 November 2019. Dashed box outlines region shown in Fig. 12d. Cross-section along line CC-CC` is shown in Figs. 12a-c. (e) As in (d) but valid for 0000 UTC 27 November 2019. Dashed box outlines region shown in Fig. 13d. Cross-section along line DD-DD` is shown in Figs. 13a-c.

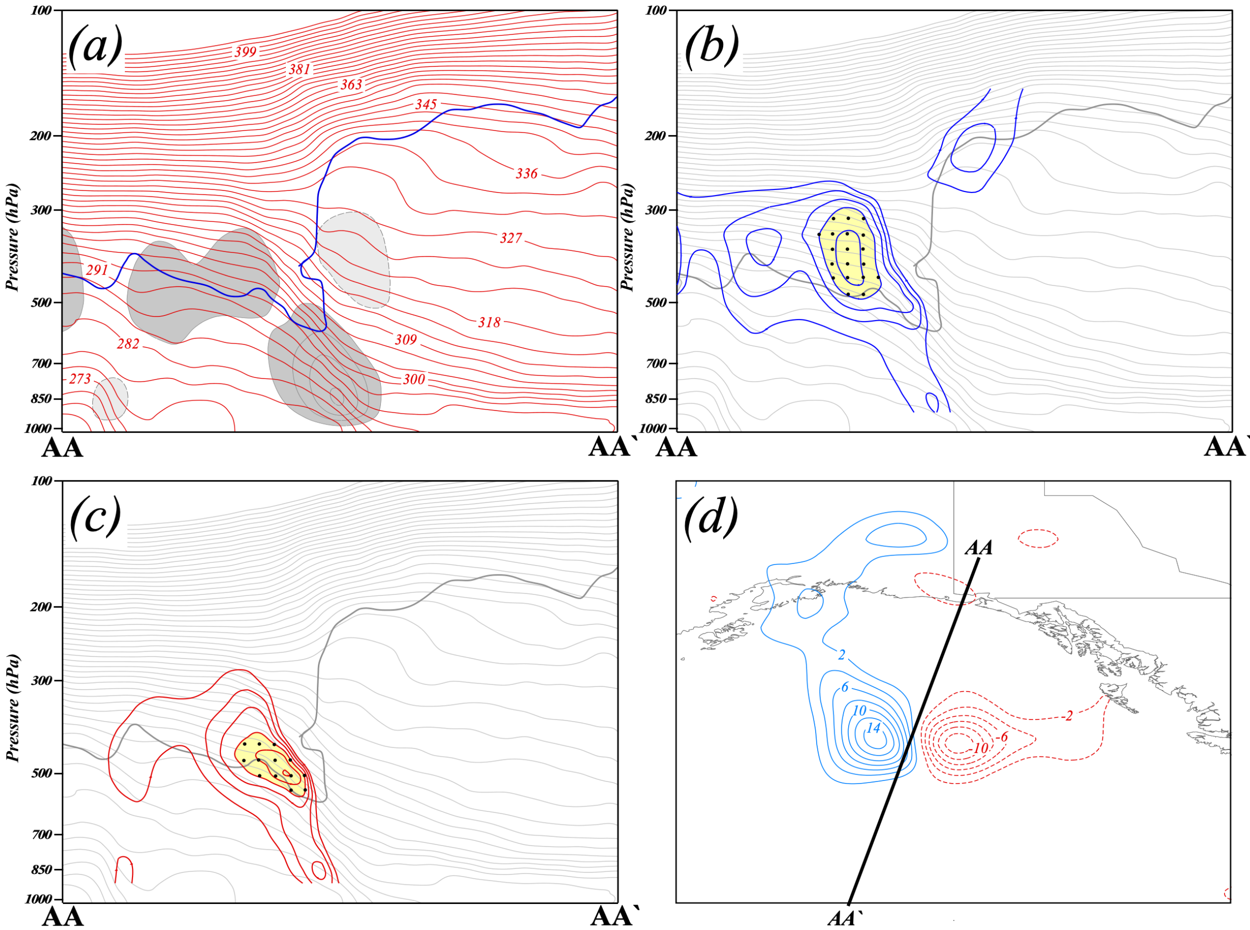

Fig. 8. (a) Cross section along AA-AA’ in Fig. 7b of the upper-level jet front system at 0600 UTC 26 November 2019. Solid, red lines are isentropes in K contoured every 3 K. Gray shading represents the total from the piecewise PV inversion with dark, solid gray indicating positive contoured every 1 dPa s^{-1} and light, dashed gray indicating negative contoured every -1 dPa s^{-1}. Dynamic tropopause, denoted by the 1.5 PV isertel, contoured in blue. (b) Tilting frontogenesis associated with the total QG-omega in Fig. 8a contoured in solid blue every 2.5 x 10^{-10} K m^{-1} s^{-1} starting at 2.5 x 10^{-10} K m^{-1} s^{-1}. Thin gray lines are isentropes as in Fig. 8a and thick gray line is the dynamic tropopause as in Fig. 8a. Values of the tilting frontogenesis at the black dots in the yellow shaded area were used in the construction of Fig. 14a. (c) Geostrophic vorticity tendency via tilting associated with the total QG-omega in Fig. 8a contoured in solid red every 2.5 x 10^{-10} s^{-2} starting at 2.5 x 10^{-10} s^{-2}. Thin and thick gray lines as in Fig. 8b. Values of the vorticity tendency via tilting at the black dots in the yellow shaded region were used in the construction of Fig. 15a. (d) 500 hPa geostrophic vorticity advection by the 300:700 hPa thermal wind. Solid blue (dashed red) contours represent NVA (PVA) labeled in m kg^{-1} s^{-1} and contoured every 2 x 10^{-17} m kg^{-1} s^{-1}. Solid black line is cross-section line AA-AA`.

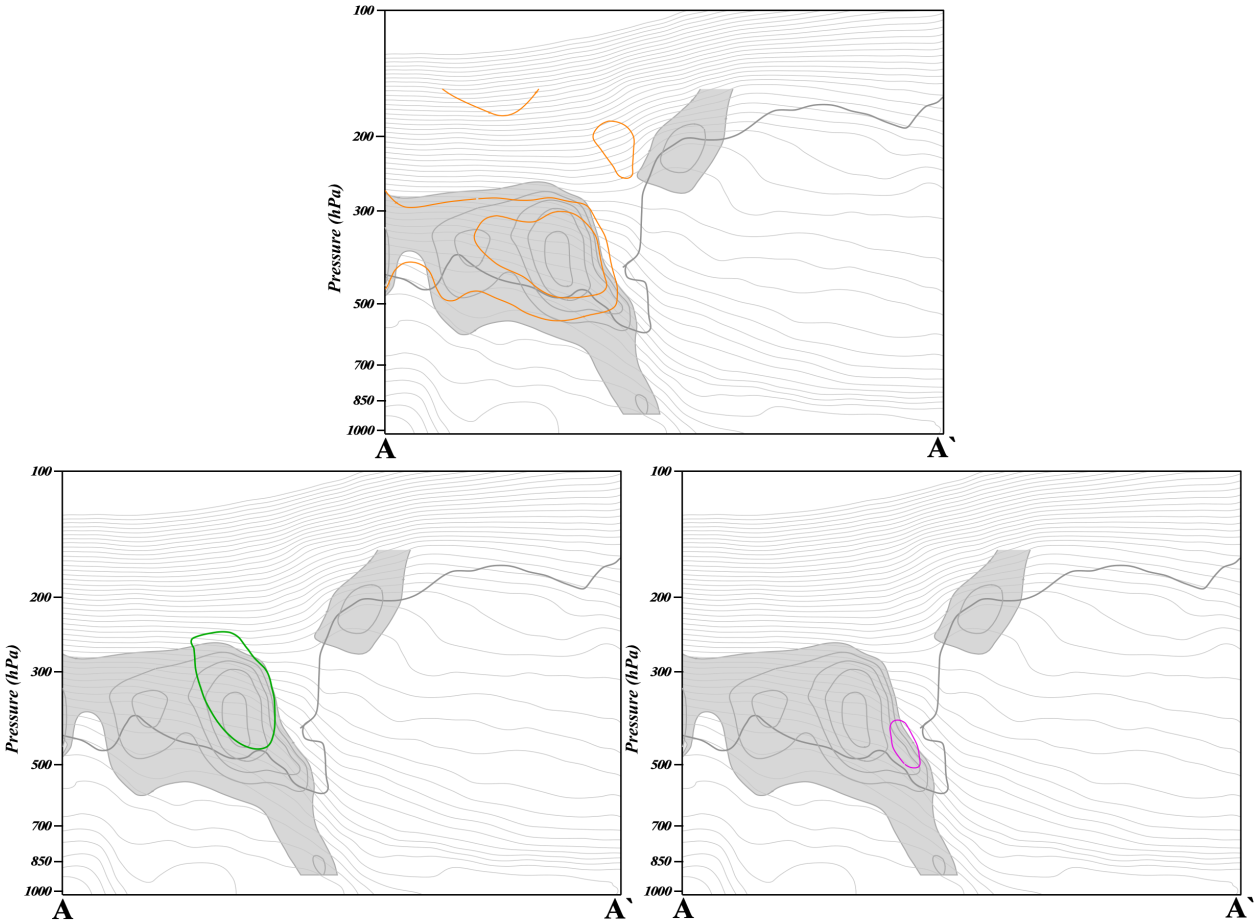

Fig. 9. (a) Tilting frontogenesis accomplished by ω_{um} and ω_{uu} valid at 0600 UTC 26 November 2019 contoured in solid orange every 2.5 x 10^{-10} K m^{-1} s^{-1} starting at 2.5 x 10^{-10} K m^{-1} s^{-1}. Light gray shading is tilting frontogenesis from the total ω as in Fig. 8b. Thin gray lines are isentropes as in Fig. 8a. (b) Tilting frontogenesis accomplished by ω_{mm} valid at 0600 UTC 26 November 2019 contoured in solid green every 2.5 x 10^{-10} K m^{-1} s^{-1} starting at 2.5 x 10^{-10} K m^{-1} s^{-1}. Light gray shading and thin gray lines as in Fig. 9a. (c) Tilting frontogenesis accomplished by the sum of ω_{im} and ω_{iu} valid at 0600 UTC 26 November 2019 contoured in solid pink every 2.0 x 10^{-10} K m^{-1} s^{-1} starting at 2.0 x 10^{-10} K m^{-1} s^{-1}. Light gray shading and thin gray lines as in Fig. 9a.

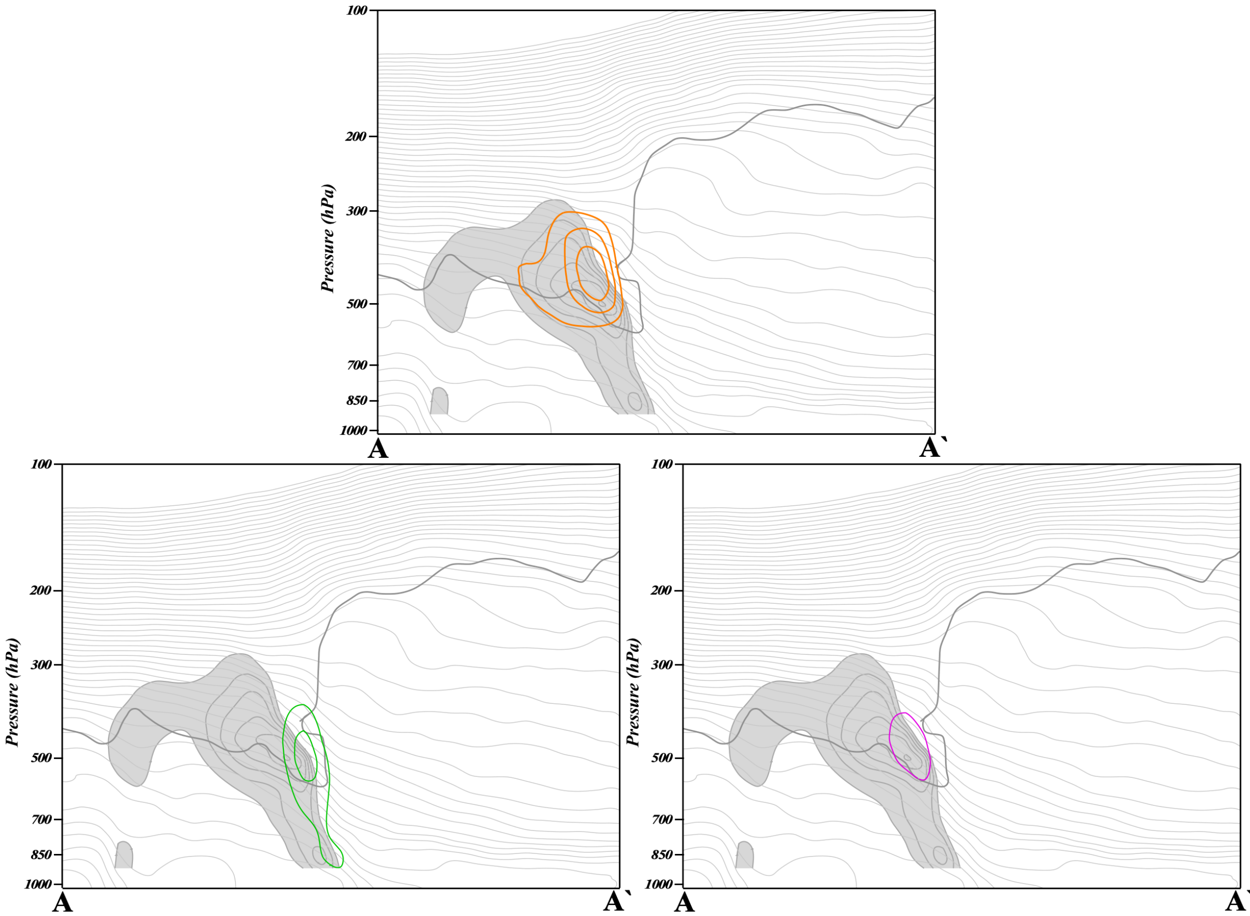

Fig. 10. (a) Geostrophic vorticity tendency via tilting accomplished by ω_{um} and ω_{uu} valid at 0600 UTC 26 November 2019 contoured in solid orange every 2.5 x 10^{-10} s^{-2} starting at 2.5 x 10^{-10} s^{-2}. Light gray shading is geostrophic vorticity tendency via tilting from the total as in Fig. 8c. Thin gray lines are isentropes as in Fig. 8a. (b) Geostrophic vorticity tendency via tilting accomplished by ω_{mm} valid at 0600 UTC 26 November 2019 contoured in solid green every 2.5 x 10^{-10} s^{-2} starting at 2.5 x 10^{-10} s^{-2}. Light gray shading and thin gray lines as in Fig. 10a. (c) Geostrophic vorticity tendency via tilting accomplished by ω_{im} valid at 0600 UTC 26 November 2019 contoured in solid pink every 2.5 x 10^{-10} s^{-2} starting at 2.5 x 10^{-10} s^{-2}. Light gray shading and thin gray lines as in Fig. 10a.

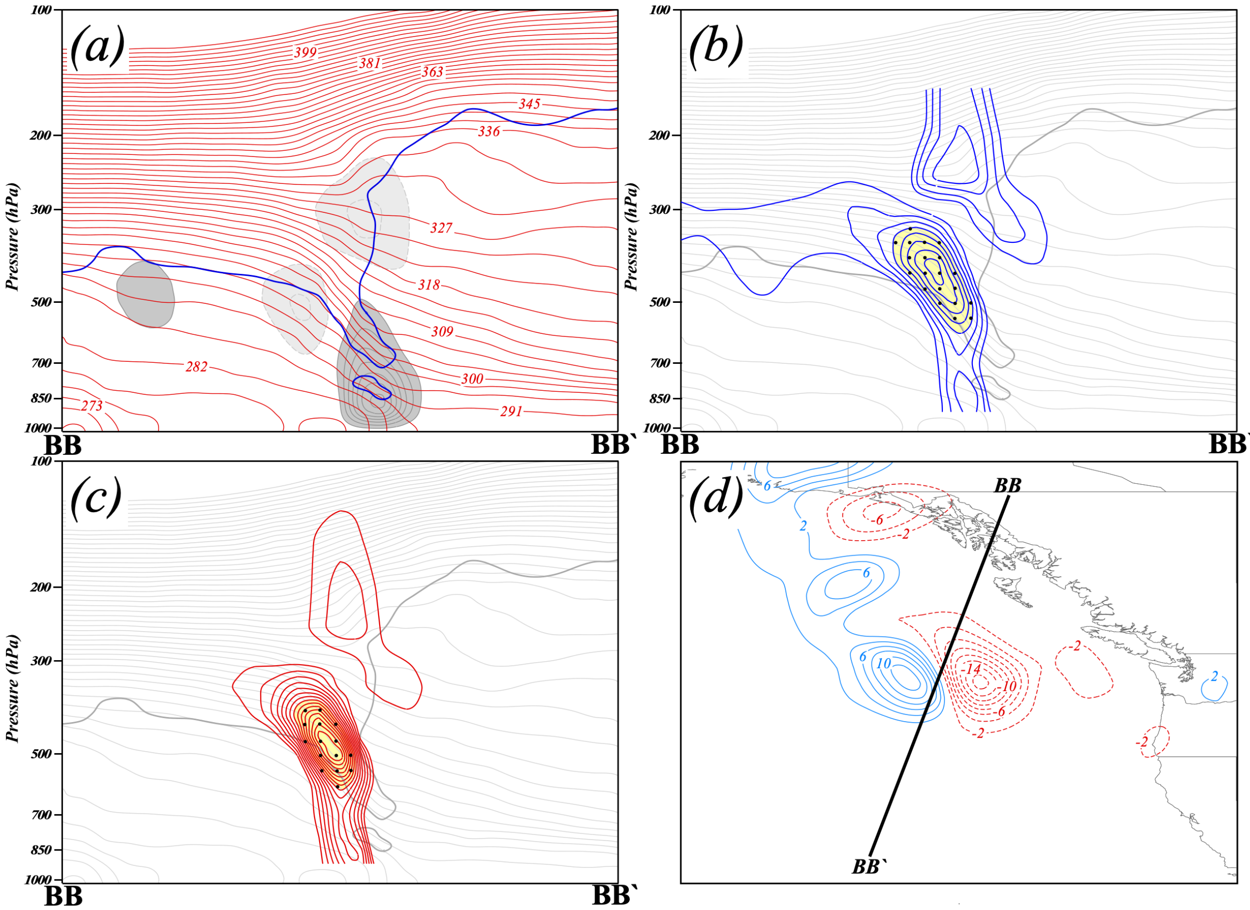

Fig. 11. Cross section along BB-BB’ in Fig. 7c of the upper-level jet front system at 1200 UTC 26 November 2019. (a) As in Fig. 8a but for 1200 UTC 26 November 2019. (b) As in Fig. 8b but for 1200 UTC 26 November 2019. (c) As in Fig. 8c but for 1200 UTC 26 November 2019. (d) As in Fig. 8d but for 1200 UTC 26 November 2019.

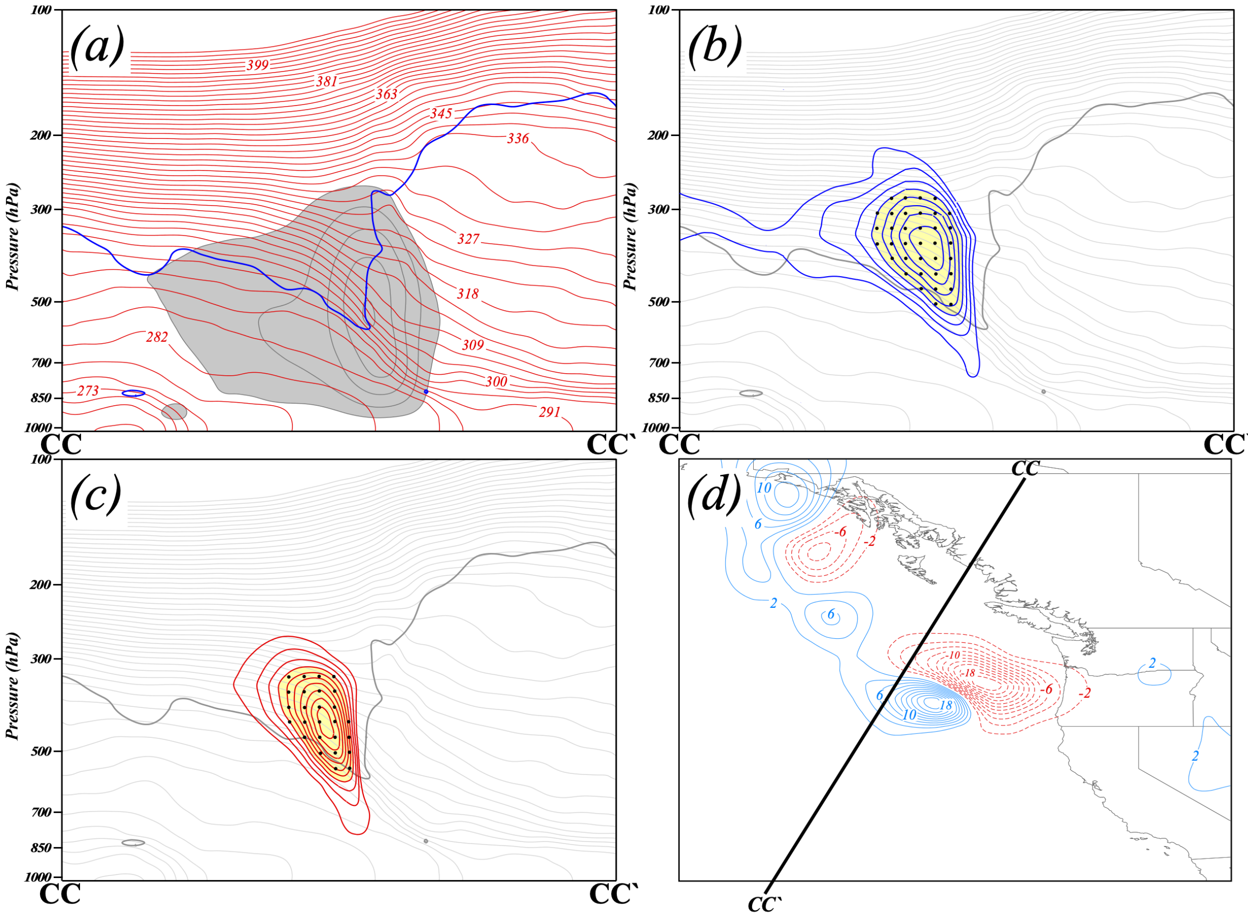

Fig. 12. Cross section along CC-CC' in Fig. 7d of the upper-level jet front system at 1800 UTC 26 November 2019. (a) As in Fig. 8a but for 1800 UTC 26 November 2019. (b) As in Fig. 8b but for 1800 UTC 26 November 2019. (c) As in Fig. 8c but for 1800 UTC 26 November 2019. (d) As in Fig. 8d but for 1800 UTC 26 November 2019.

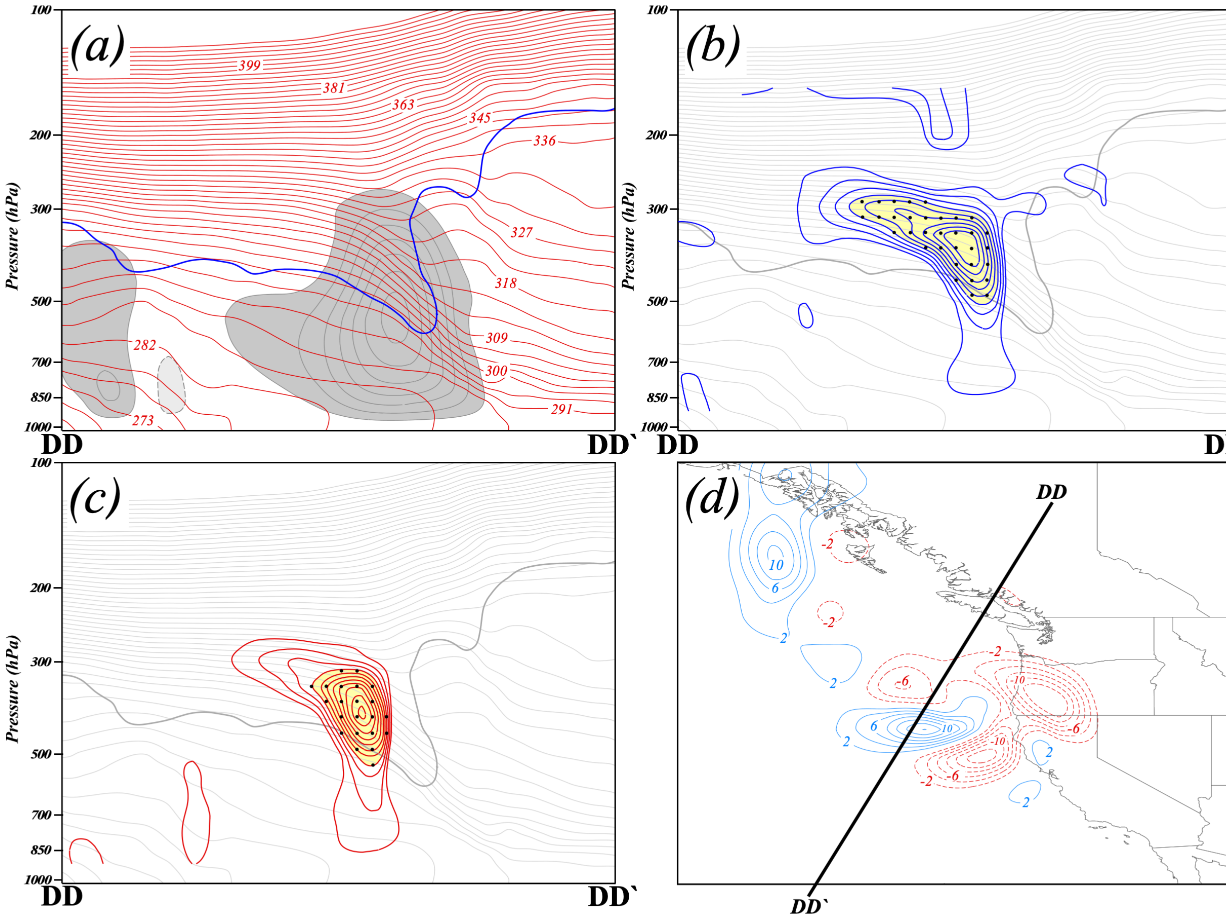

Fig. 13. Cross section taken along DD-DD' in Fig. 7e of the upper-level jet front system at 0000 UTC 27 November 2019. (a) As in Fig. 8a but for 0000 UTC 27 November 2019. (b) As in Fig. 8b but for 0000 UTC 27 November 2019. (c) As in Fig. 8c but for 0000 UTC 27 November 2019. (d) As in Fig. 8d but for 0000 UTC 27 November 2019.

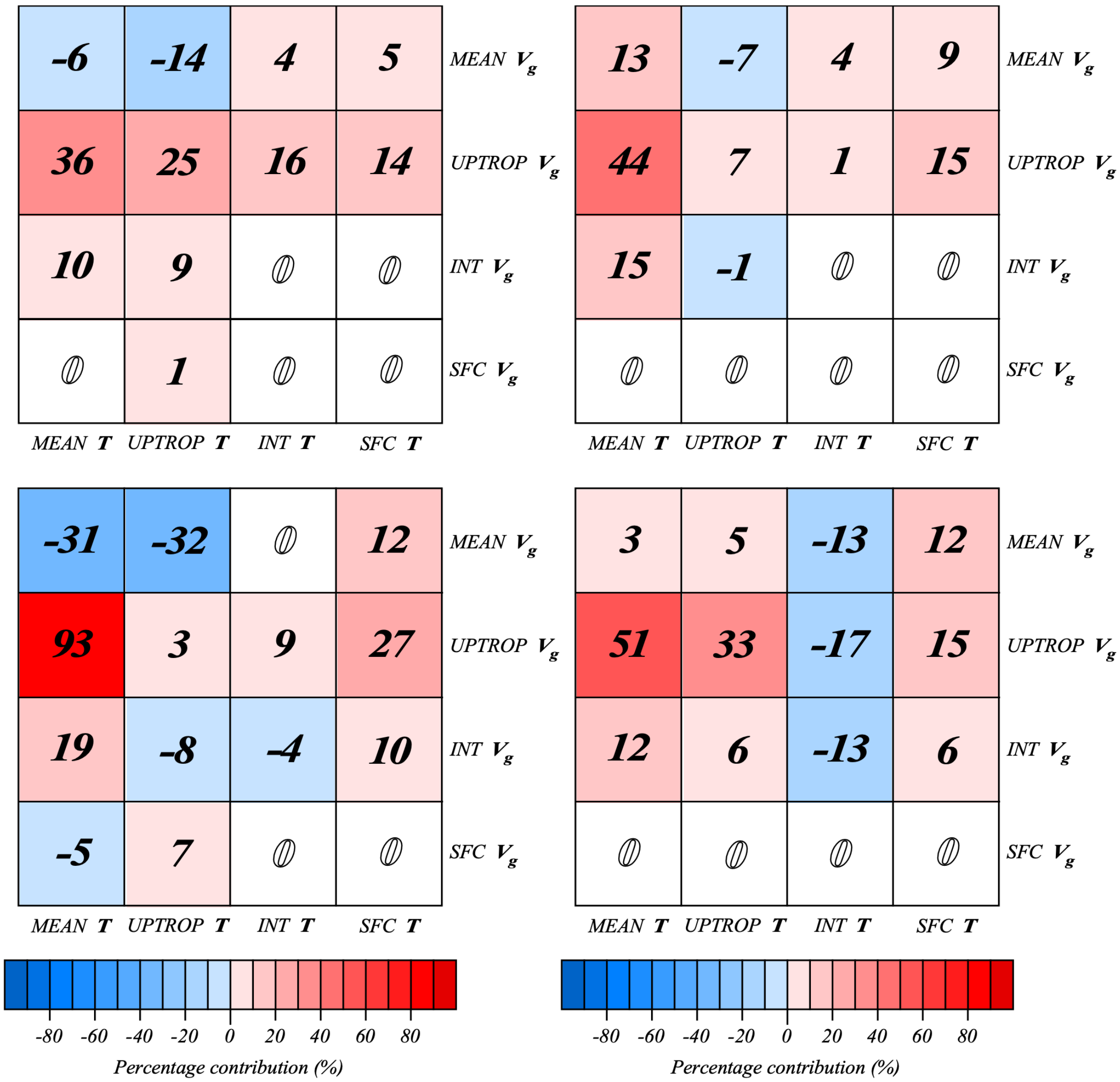

Fig. 14 - (a) Percentage contribution of total tiliting frontogenesis by QG-omega species along line A-A’ in Fig. 7b at 0600 UTC 26 November 2019. (b) As for Fig. 14a but as measured along line B-B’ in Fig. 7c at 1200 UTC 26 November 2019. (c) As for Fig. 14a but as measured along line C-C’ in Fig. 7c at 1800 UTC 26 November 2019. (d) As for Fig. 14a but as measured along line D-D’ in Fig. 7e at 0000 UTC 27 November 2019.

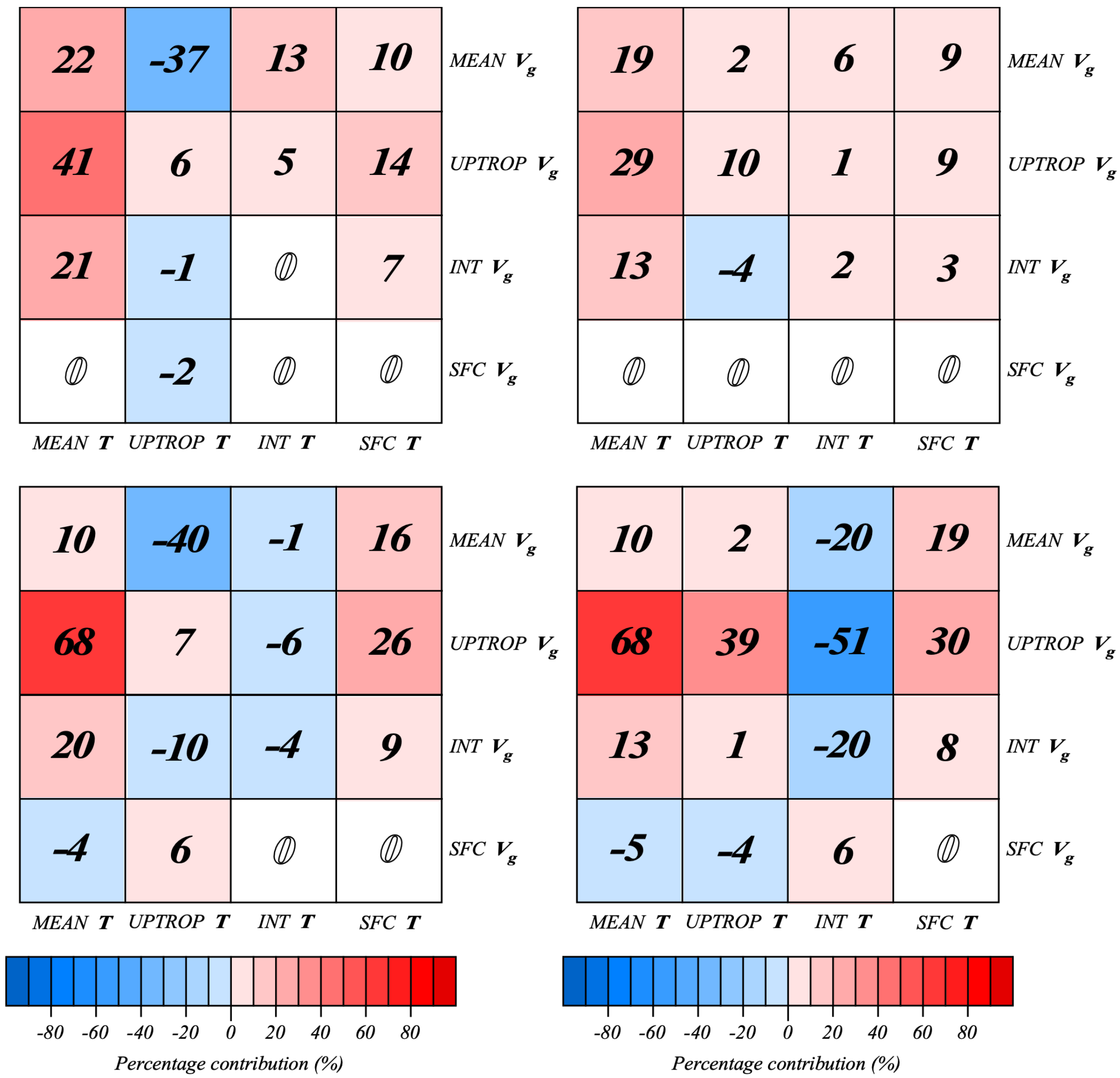

Fig. 15 (a) Percentage contribution of total vorticity production via tilting by QG-omega species along line A-A' in Fig. 7b at 0600 UTC 26 November 2019. (b) As for Fig. 15a but as measured along line B-B' in Fig. 7c at 1200 UTC 26 November 2019. (c) As for Fig. 15a but as measured along line C-C' in Fig. 7c at 1800 UTC 26 November 2019. (d) As for Fig. 15a but as measured along line D-D' in Fig. 7e at 0000 UTC 27 November 2019.

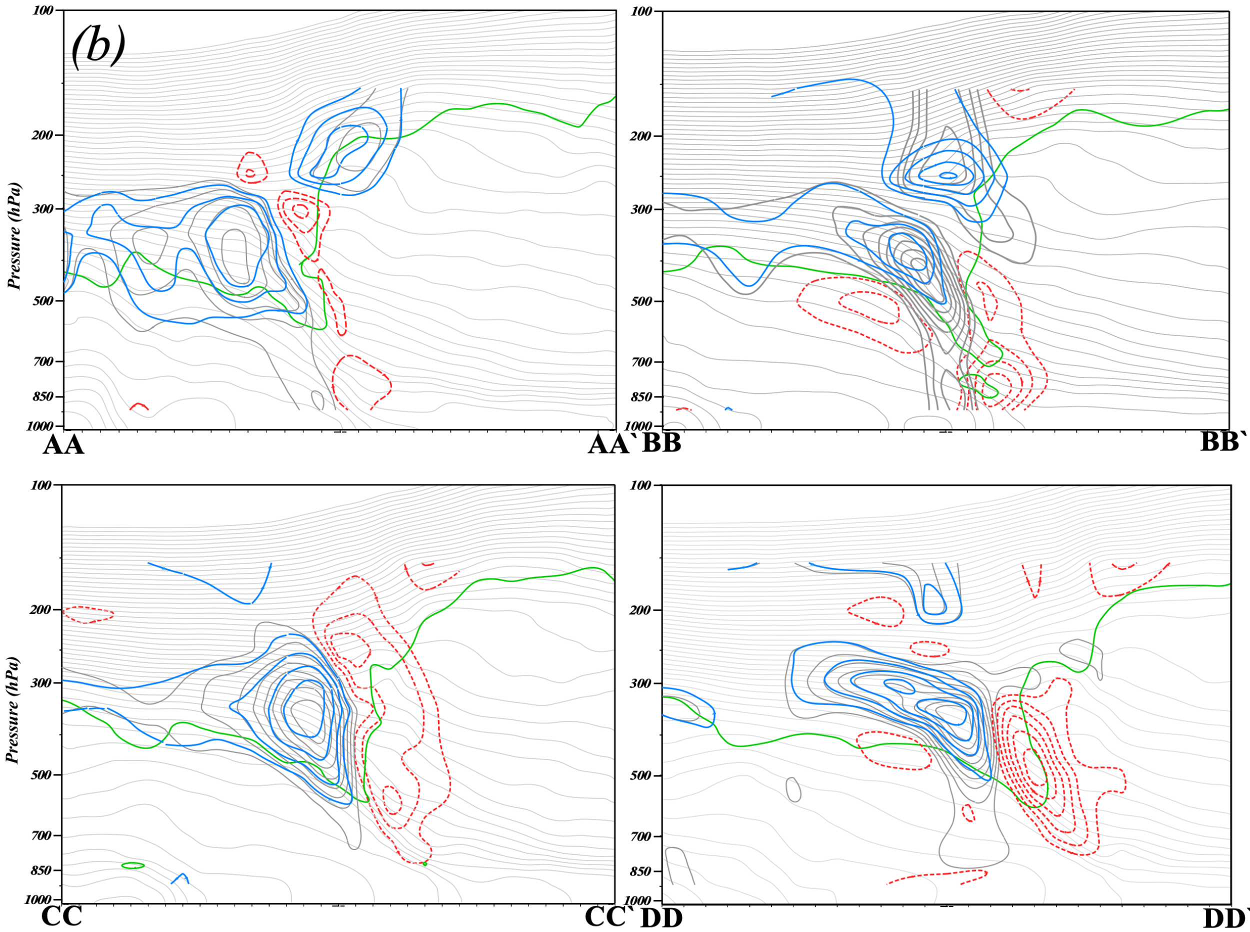

Fig. 16 (a) Tilting frontogenesis (dark gray), total 3D geostrophic frontogenesis (red for negative, blue for positive), theta (light gray) and 1.5 PVU isertel along the cross-section shown in Fig. 8c at 0600 UTC 26 November. (b) As for Fig. 16a but for 1200 UTC 26 November along the cross section line shown in Fig. 11c. (c) As for Fig 16a but for 1800 UTC 26 November along the cross-section line shown in Fig. 12c. (d) As for Fig. 16a but for 0000 UTC 27 November along the cross-section line shown in Fig. 13c. Frontogenesis is shown in units of 10^{-10} K m^{-1} s^{-1} and contoured every
2.5 x 10^{-10} K m^{-1} s^{-1}.

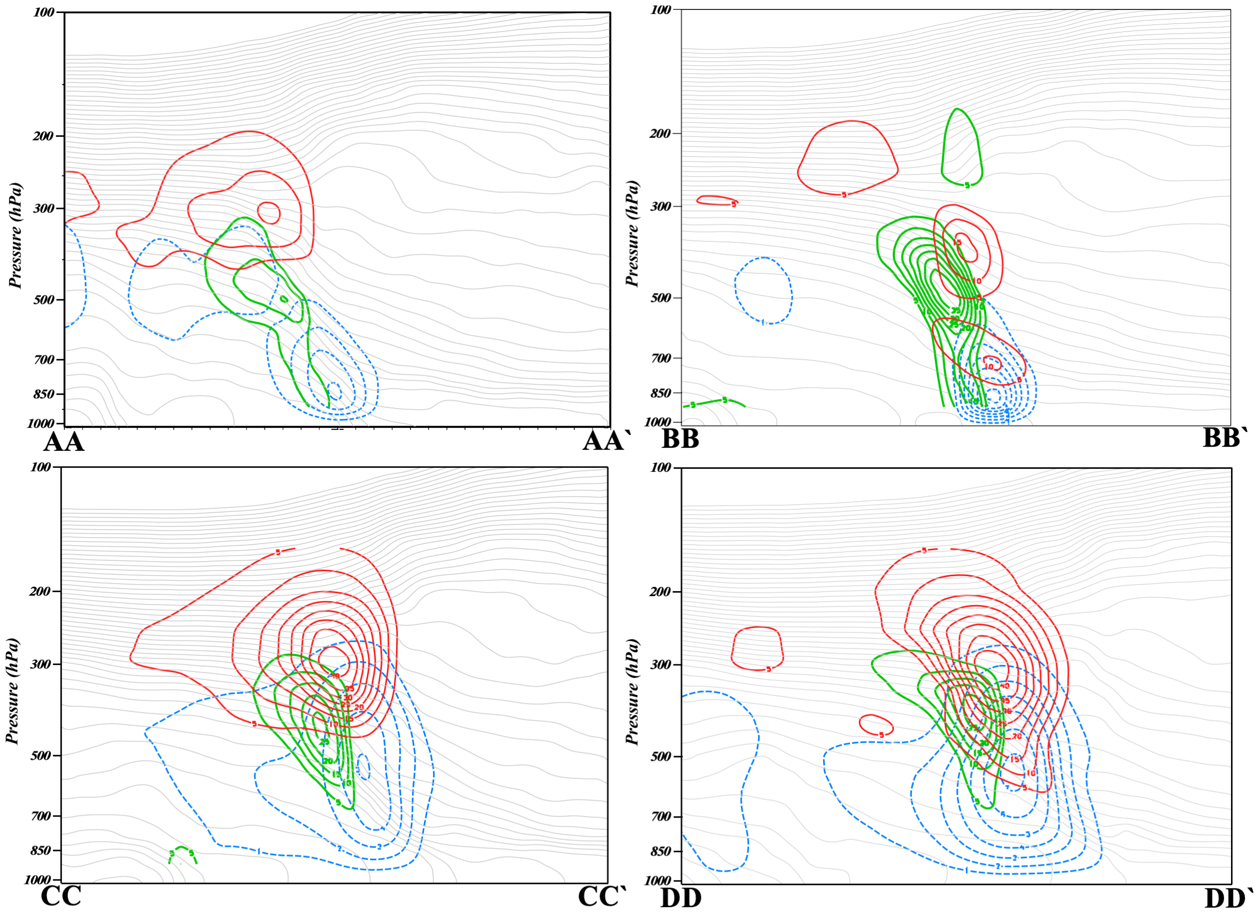

Fig. 17 (a) Tilting vorticity tendency (green), stretching tendency (red), theta (light gray) and QG subsidence (positive omega, dashed blue) along the cross-section shown in Fig. 8c at 0600 UTC 26 November. Vorticity tendencies in units of 5 x 10^{-10} s^{-2}. (b) As for Fig. 17a but for 1200 UTC 26 November along the cross section line shown in Fig. 11c. (c) As for Fig 17a but for 1800 UTC 26 November along the cross-section line shown in Fig. 12c. (d) As for Fig. 17a but for 0000 UTC 27 November along the cross-section line shown in Fig. 13c.

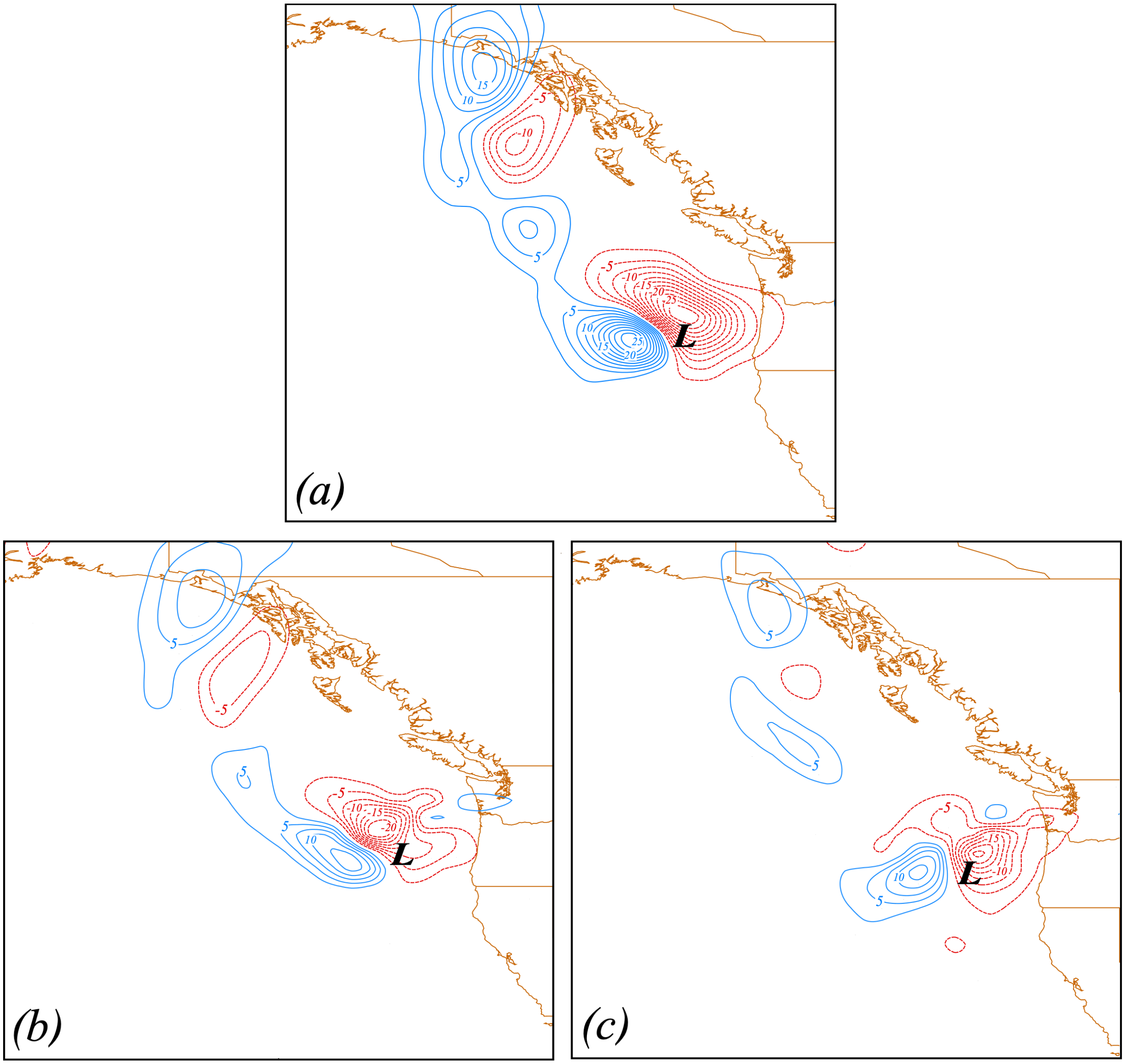

Fig. 18 (a) 500 hPa geostrophic vorticity advection by the 300:700 hPa thermal wind at 1800 UTC 26 November 2019. PVA (NVA) by the thermal wind indicated by the dashed red (solid blue) contours labeled in m kg^{-1} s^{-1} and contoured every 2.5×10^{-17} m kg^{-1} s^{-1} starting at 2.5×10^{-17} m kg^{-1} s^{-1} (-2.5×10^{-17} m kg^{-1} s^{-1}). "L" indicates position of sea-level pressure minimum at 1800 UTC 26 November 2019. (b) As for Fig. 18a but for 500 hPa geostrophic shear vorticity advection by the 300:700 hPa thermal wind. Isopleths labeled and contoured as in Fig. 18a. (c) As for Fig. 18a but for 500 hPa geostrophic curvature vorticity advection by the 300:700 hPa thermal wind. Isopleths labeled and contoured as in Fig. 18a.